Draft of July 13, 2021

Published as:

Poulaki EM, Stockli DF, Flansburg ME, Gevedon ML, Stockli LD, Barnes JD, Soukis K, Kitajima K, Valley JW (2021) Zircon U-Pb and geochemical signatures in high-pressure, low-temperature metamorphic rocks as recorders of subduction zone processes, Sikinos and Ios islands, Greece. Chem Geol 582: doi.org/10.1016/j.chemgeo.2021.120447

Zircon U-Pb and geochemical signatures in high-pressure, low-temperature metamorphic rocks as recorders of subduction zone processes, Sikinos and Ios islands, Greece

Authors: Eirini M. Poulaki[1], Daniel F. Stockli[1], Megan E. Flansburg[1], Michelle L. Gevedon[2], Lisa D. Stockli[1], Jaime D. Barnes[1], Konstantinos Soukis[3], Kouki Kitajima[4], and John W. Valley[4]

[1]Dept. of Geological Sciences, University of Texas at Austin, USA
[2]Colorado College, USA
[3]National and Kapodistrian University of Athens, Greece
[4]Dept. of Geoscience, University of Wisconsin, Madison, WI, 53706, USA

Corresponding author: Eirini Poulaki (eirini_poulaki@utexas.edu)

Highlights:

- Zircon 2D U-Pb maps constrain the spatial domains of polymetamorphic zircon grains.
- Two phases of subduction metamorphism are recorded by zircon rims on Sikinos and Ios.
- Eocene rims formed by recrystallization/precipitation under HP/LT metamorphism.
- Oligocene rims record fluids from dehydrating sediments off the subducting slab.

- The CBU/CB contact has not experienced large displacements at least since the Eocene.

Abstract

Zircon U-Pb dating is a powerful and widely used geochronologic technique to constrain the timing and rates of magmatic and high and lower-grade metamorphic processes, as well as sediment provenance. Zircon trace element (TE) compositions also record magmatic and metamorphic processes during zircon growth. In this study, zircon laser ablation split-stream (LA-SS)-ICP-MS U-Pb and TE depth-profiling and novel two-dimensional zircon mapping techniques are used in combination with oxygen isotope analyses (secondary ion mass spectrometry, SIMS) to reconstruct the timing and metamorphic conditions recorded by recrystallization and growth of zircon rims, which provide valuable insight into the petro-tectonic evolution of high-pressure/low-temperature (HP/LT) metamorphic rocks formed in subduction zones. These techniques are applied to zircon grains from HP/LT metamorphic rocks of the Cycladic Blueschist Unit (CBU) and Cycladic Basement (CB) on Sikinos and Ios islands, Greece, which experienced metamorphism and deformation associated with subduction and subsequent back-arc exhumation. Zircon records multiple episodes of non-magmatic zircon rim growth at ~50 Ma and ~26 Ma. Eocene metamorphic rims are associated with HP/LT metamorphism and are observed in both units, suggesting likely juxtaposition prior to or during subduction and associated HP metamorphism. The similarity between TE concentrations and $\delta^{18}O$ values of the Eocene rims and their corresponding cores is an indicator for re-crystallization and precipitation as a mechanism of zircon growth. In contrast, Oligocene zircon rims appear to be restricted to a <0.5 km thick zone along the CB-CBU contact, characterized by garnet break-down, and show HREE enrichment and higher $\delta^{18}O$ values in the rims compared to the cores, consistent with a model suggesting metasomatic infiltration of fluids derived from dehydrating sedimentary rocks during progressive subduction and underplating prior to back-arc extension. This metamorphism appears to be static

in nature and does not support major late Cenozoic reactivation of the contact as an extensional shear zone during back-arc extension.

Key words: Metamorphic zircon; Cyclades, Subduction zone metamorphism; Zircon Trace elements; Zircon U-Pb; Zircon $\delta^{18}O$; two-dimensional elemental maps

1. INTRODUCTION

Subduction has recycled oceanic lithosphere throughout much of Earth's history and is thus critical for long-term element and volatile cycling. Although some convergent margin processes, such as seismicity or arc magmatism are well studied and have been of paramount importance in the formulation of the plate tectonics paradigm, most structural, metamorphic, and metasomatic processes related to subduction are obscured due to continued overprinting and recycling into the mantle. In particular, processes happening along the subduction interface, including meso- and micro-scale deformation and concomitant metamorphism operating along the plate interface in subduction zones, are not directly accessible. However, exhumed subduction complexes, exposed by either progressive subduction, back-arc extension, or subsequent continental collisions, provide an opportunity to investigate the temporal, structural, metamorphic, thermal and rheological evolution of convergent margins (e.g., Agard et al., 2018; Bebout and Penniston-Dorland, 2016; Brun and Faccenna 2007; Cloos, 1993; Vannucchi et al., 2008). Detailed integration of isotopic and elemental microanalyses provide insight to the metamorphic conditions of these events during prograde and retrograde P-T paths within subduction complexes.

Zircon U-Pb dating is a well-established and robust geochronological technique widely used to determine the crystallization ages of igneous rocks and detrital provenance age spectra of sedimentary rocks. Although zircon was traditionally viewed as a highly refractory phase, it has recently been shown that, depending on the protolith composition, zircon can recrystallize and record various metamorphic reactions and rock-fluid interactions (e.g., Kohn and Kelly, 2018). Over the last 20 years, various studies have tried to understand the nature of metamorphic zircon rims by using U-Pb and trace element (TE) analyses (e.g., Kohn and Kelly 2018; Rubatto, 2017). In particular, advances in micrometer-scale spot analytical techniques reveal a more detailed picture of the geologic history recorded by radiometric ages and trace-element chemical composition of zircon in metamorphic rocks (e.g., Kylander-Clark 2017; Schmitt and Vazquez 2017; Page et al. 2014, 2019). These micrometer-scale spot techniques are particularly useful to investigate high-grade and multi-stage metamorphism (e.g., Chen et al., 2010; Kelly and Harley, 2005; Yuan et al., 2008; Whitehouse and Platt, 2003). The timing of these events can be constrained by radiometric dating of the rims (e.g., Odlum and Stockli, 2019; Seymour et al., 2016).

Laser ablation inductively coupled plasma mass spectrometry (LA-ICP-MS) and secondary ion mass spectrometry (SIMS) methods combined with cathodoluminescence images provide the spatial resolution necessary to investigate complex zircon growth zones. In this study, we apply zircon U-Pb and TE depth profile analysis, two-dimensional age mapping, and oxygen isotope analyses to distinguish multiple generations of zircon growth and to better understand the metamorphic processes affecting high-pressure rocks during subduction and exhumation in the Southern Cyclades, Greece. In previous studies, a total of 141 samples were collected from both Sikinos and Ios and analyzed by zircon U-Pb depth-profiling (Flansburg et al., 2019; Poulaki et al., 2019); 42 of these samples exhibited resolvable zircon overgrowths of ~26 Ma and/or ~50 Ma and they are the focus of this study. Sikinos and Ios islands in the southern Cyclades, Greece (Fig.1) are part of a metamorphic core complex in the back-arc of the Hellenic subduction zone and have experienced subduction, subsequent exhumation, and arc magmatism (e.g., Jolivet & Brun, 2010; Pe-Piper & Piper, 2007). The Aegean domain has a well-constrained geologic setting, which provides the necessary geologic context to determine when and under what metamorphic conditions zircon rims form. This work provides further constraints on how metamorphic zircon forms during subduction related metamorphism and the sources of the fluids during exhumation, as well as the nature of the contact between the Cycladic Basement (CB) and the Cycladic Blueschist Unit (CBU).

2. GEO-CHEMISTRY AND ISOTOPIC SYSTEMATICS OF METAMORPHIC ZIRCON

The exact conditions necessary for metamorphic zircon rim formation during HP/LT metamorphism are widely debated. Studies propose that zircon rims can form during prograde, retrograde, and/or at peak metamorphism (Bingen et al. 2001; Hermann and Rubatto 2003; Kelly and Harley 2005; Kohn and Kelly 2018; Rubatto 2002; Schaltegger et al. 1999; Vavra et al. 1999). In contrast, other work suggests that zircon rim formation does not strongly depend on pressure and temperature conditions, but rather is controlled by the surrounding mineral and fluid phases (Geisler et al. 2007; Hoskin 2005; Hoskin and Schaltegger 2003; Rubatto, 2017). The equilibrium mineralogic assemblage of metamorphic rocks undergoes many complex prograde and retrograde phase transformations. Since zircon can be stable over a large range of P-T conditions, it can have equilibrated with phase assemblages that are no longer present in the preserved rock, such as garnet and feldspar.

123 However, metamorphic zircon grains preserve a large range of TE concentrations that can
124 be used as indicators for their metamorphic origin. A common proxy used to differentiate
125 magmatic from metamorphic zircon is Th/U, which is commonly less than 0.1 for metamorphic
126 rocks (Williams et al., 1996; Williams, 2001; Rubatto, 2002). However, use of Th/U<0.1 to
127 discriminate between magmatic and metamorphic zircon can be misleading and should be used
128 with caution since Th-rich accessory phases (e.g., allanite and monazite) strongly influence bulk
129 rock Th budgets (e.g., Harley et al., 2007; Kelly & Harley, 2005; Korhonen et al., 2013; Rubatto,
130 2017; Vavra et al., 1999; Yakymchuk et al. 2018). The incorporation of REEs and TEs released
131 by the breakdown of surrounding mineral phases allows individual stages of zircon growth to be
132 associated with specific metamorphic P-T conditions (e.g., Kelly and Harley, 2005; Rubatto and
133 Hermann, 2003; Schaltegger et al., 1999).

134 The growth of coeval minerals such as garnet, monazite, and feldspar can regulate the REE
135 concentrations in metamorphic zircon (e.g., Murali et al., 1983; Rubatto, 2002; Schaltegger et al.,
136 1999). For instance, zircon forming in the presence of feldspar yield negative Eu anomalies (e.g.,
137 Kohn, 2016; Rubatto 2002; Schaltegger et al. 1999) and zircon depleted in light and medium REEs
138 (LREE and MREE) may form in the presence of titanite, allanite, or monazite (Rubatto et al. 2009).
139 In addition, zircon formed during HP/LT metamorphism in the presence of garnet would be
140 depleted in HREE (e.g., Rubatto, 2017). However, zircon formed in the absence of minerals that
141 dominate REE budgets, such as garnet, may have TE and REE concentrations that reflect complex
142 changes in zircon geochemistry during metamorphic paragenesis.

143 Oxygen isotope ($\delta^{18}O$) ratios in metamorphic zircon can provide crucial information about
144 the sources of fluids present at the time of zircon formation. High-precision SIMS analyses capture
145 oxygen isotope variability between zircon cores and rims, allowing for identification of magmatic
146 and metamorphic provenance and the role of externally derived fluids in metamorphic zircon
147 growth (e.g., Valley, 2003; Rubatto, 2017; Kohn and Kelley, 2018; Martin et al., 2006; Page et al.,
148 2019). In this study, the integration of U-Pb ages (including U-Pb age maps), trace elements, and
149 oxygen isotope ratios of metamorphic zircon rims reveal the timing and concomitant fluid
150 evolution of prograde and retrograde metamorphism in the southern Cyclades.

3. GEOLOGIC SETTING

The Attico-Cycladic complex is one of the most exceptional places where subduction zone rocks are exposed at the surface. The exposed subduction complex rocks are located in the upper plate of the Hellenic subduction zone and were exhumed during back-arc extension in the late Cenozoic due to continued subduction and slab-rollback (e.g., Jolivet & Brun, 2010; Papanikolaou 2013; Pe-Piper & Piper, 2002; Ring et al., 2010; Royden, 1993). This regional two-stage exhumation event consisted of buoyancy-driven underplating during Eocene subduction and later Miocene core-complex style extension triggered by trench retreat and rollback of the African slab. The final stages of exhumation were accommodated along low-angle normal faults in late Miocene time (Coleman et al., 2019; Jolivet & Brun, 2010; Lister et al., 1984; Papanikolaou, 2013; Ring et al., 2010; Schneider et al., 2011; Schneider et al., 2018; Soukis & Stockli, 2013).

Eocene HP/LT metamorphism is documented on many Cycladic islands; age constraints consist of: $^{40}Ar/^{39}Ar$ white mica ages of ~45 ± 5 Ma of blueschist metamorphism on Naxos (Andriessen et al., 1979; Wijbrans and McDougall, 1986, 1988), and white mica Rb/Sr and $^{40}Ar/^{39}Ar$ ages and garnet Sm-Nd ages of ~49 to 55 Ma for peak HP/LT metamorphism on Syros, Sifnos, Tinos, and Ios islands (Baldwin and Lister, 1998; Bröcker et al., 1993, 2013; Clift et al., 2017; Dragovic et al., 2015; Lagos et al., 2007; Lister and Forster, 2016; Tomaschek et al., 2003). Subsequent greenschist facies metamorphism has been attributed to early syn-subduction exhumation following southward migration of the magmatic arc and contemporaneous exhumation during back-arc extension. Commencement of large-scale continental extension in the central Aegean has been suggested to occur at ~23 Ma (e.g., Lister et al., 1984; Ring et al., 2010). Numerous studies have shown that activity along the West and North Cycladic detachment started in the Miocene (e.g., Jolivet et al., 2010; Grasemann et al., 2012, Soukis and Stockli, 2013). On Naxos, the age of greenschist-facies retrogression has been proposed at ~25 to ~20 Ma (Andriessen et al., 1979; Andriessen, 1991), ~27 to ~ 19 Ma (Wijbrans and McDougall 1988), or at ~23 to ~20 Ma (Duchêne et al. 2006). On Syros, during the later stages of exhumation, it has been proposed that the CBU interacted with aqueous fluids at ~25 to ~35 km (Miller et al., 2009). Recent studies show that Syros experienced greenschist facies metamorphism with temperatures from 500-400ºC according to quartz-calcite oxygen isotope thermometry in epidote boudin necks (Cisneros et al., 2021), and indicate deformation during dynamic greenschist facies occurred around ~36 Ma based on Rb-Sr isochron (Kotowski et al., 2021). On Tinos, the Oligocene-Miocene greenschist facies

overprint is estimated to result from temperatures of ~400 to 500ºC and pressures from 4 to 9 kbar (Bröcker et al., 1993). Further north in Evvia and Samos islands, the Basal Unit tectonically underlies the CBU (Papanikolaou 1979; Ring et al., 1999, 2001). The Basal Unit is a Mesozoic-early Cenozoic meta-carbonate sequence with an Eocene meta-flysch that has experienced a Miocene (Ring et al., 2001) or Oligocene HP metamorphism (Bröcker et al., 2004).

In the southern Cyclades, Sikinos and Ios islands contain exposures of the CB and the overlying metasedimentary CBU (Fig.1). The CB is composed of a suite of heterogeneously deformed Carboniferous granitoids, and aplitic dikes intruded into quartzo-feldspathic schist and garnet mica schist basement metasedimentary rocks with maximum depositional ages (MDAs) from Neoproterozoic to Carboniferous (Flansburg et al., 2019; Keay and Lister, 2002; Poulaki et al., 2019; van der Maar & Jansen, 1983; Zlatkin et al., 2018). On both Ios and Sikinos, the CBU is composed of Permian to Cretaceous metasedimentary and meta-volcanic rocks (Flansburg et al., 2019; Poulaki et al., 2019). The CBU on both islands contains meta-basic lithologies, quartz mica schist, calc-schist, garnet-glaucophane-bearing schist and calcitic to dolomitic marble. The P-T estimates for the HP/LT metamorphism on Ios and Sikinos vary widely, including estimates of 25 kbar at 540°C (Perraki and Mposkos, 2001), 18.5 ± 3 kbar at 510 ± 20°C (Augier et al., 2015; Huet et al., 2009), and 11 kbar at 475°C (Gupta and Bickle, 2004). The timing of peak HP/LT metamorphism has been estimated at ~50 to ~40 Ma, whereas the greenschist facies metamorphism is defined at ~20 to ~30 Ma based on $^{40}Ar/^{39}Ar$ dating of white mica and K-feldspar (e.g., Baldwin and Lister, 1998; Forster et al., 2020). We apply integrated geochemical and geochronometric methods to both the CB and CBU to understand their multi-stage evolution and set further constraints on the nature of the contact between the two units.

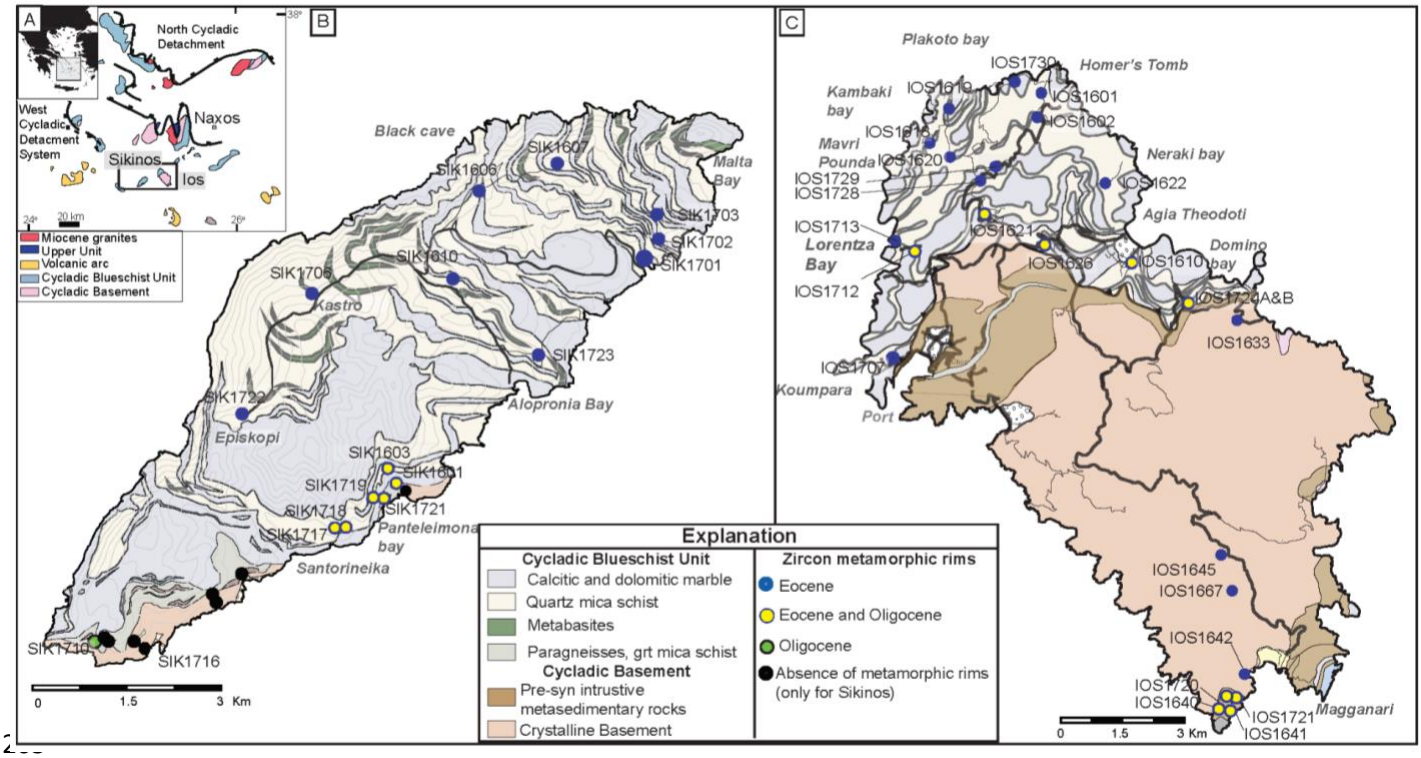

Figure 1: a) Tectonic map of the Attic-Cycladic area (Grasemann et al., 2012; Jolivet & Brun, 2010). (b) Geological map of Sikinos Island from Poulaki et al. (2019). (c) Geological map of Ios Island from Flansburg et al. (2019). Sample location symbols for both (b) and (c) represent the presence or absence of zircon metamorphic rims. Blue dots indicate samples with Eocene zircon rims. Blue/Yellow dots indicate samples with Oligocene and Eocene zircon rims.

4. METHODOLOGY

A series of methodological steps is used to characterize the age and geochemistry of zircons collected from the CBU and CB of Sikinos and Ios. LA-ICP-MS depth-profiling analyses of unpolished zircon grains (length from 80 to 200 μm) adhered to a tape mount yield one-dimensional chemical and isotopic profiles (Marsh & Stockli, 2015) and allow for discrimination of zircon rims (overgrowths) from magmatic cores. Due to the multistage metamorphic evolution of these rocks, zircon depth-profiling allows us to discern age zonation that could not be analyzed if the grain was polished, since these zones are often very thin (<10 μm) and are typically removed to expose cores of polished zircon. Samples that exhibit non-magmatic overgrowths were further analyzed by using laser ablation split-stream (LA-SS)-ICP-MS to simultaneously measure a profile of U-Pb age and trace element concentrations from the rim into the core (Fig. 2). Selected zircon grains were mounted in epoxy, polished, and CL imaged prior to the measurement of oxygen isotope ratios via SIMS to evaluate the potential fluid sources involved in late-stage metamorphic

zircon growth. Finally, two-dimensional U-Pb age maps were generated for select grains to better understand the zircon morphology, zonation, and isotopic heterogeneity.

4.1 Zircon U-Pb and TE depth profile (LA-SS)-ICP-MS analyses

Depth-profiling (LA-SS)-ICP-MS analyses on zircon grains was conducted using a Photon Machines Teledyne Analyte G.2 193nm Excimer laser and two Thermo Element2 HR-ICP-MS following procedures from Marsh and Stockli (2015) at the UTChron Laboratories, University of Texas at Austin. U-Pb depth profiles were constructed with single 30 μm spots ablated for 30 seconds with an energy of 4 mJ and repetition rate of 10 Hz. Ablation rates of 0.5 μm/sec result in profiles of the outer ~15 μm of each grain. Zircon rims were distinguished from cores during data reduction by the presence of a step function in the elemental concentrations and age and by selecting a well-defined "plateau" in the $^{206}Pb/^{238}U$ final age. Zircon standard GJ1 was used as the primary reference material (601.7 ± 1.3 Ma; Jackson et al., 2004) and Plešovice (337.1 ± 0.4 Ma; Sláma et al., 2008) was used as a secondary standard. Data were reduced using the VisualAge Data Reduction Scheme addition to Iolite v3.7 (Paton et al., 2011; Petrus and Kamber, 2012). Zircon rim ages with more than 30% discordance between $^{206}Pb/^{238}U$ and $^{207}Pb/^{235}U$ ages were discarded; ages are reported with 2-sigma propagated errors. Zircon U-Pb data from metasedimentary samples are plotted with Kernel Density Estimate (KDE) histograms (Vermeesch, 2012) using the detritalPy Python script (Sharman et al., 2018).

For TE analyses, NIST612 glass was used as the primary reference material and AusZ2 zircon as the secondary standard (Kennedy et al., 2014). The stoichiometric concentration of silicon in zircon (15.32%) was used for internal standardization of TE concentrations. Data reduction utilized the Trace Element_IS Data Reduction Scheme in Iolite (Woodhead et al., 2007). U-Pb and TE depth profile data from the two mass spectrometers were synced, allowing for precise correlation. The entire continuous 30 sec ablation trace was parsed into 1-sec increments (0.5μm/sec), exported and chondrite normalized (McDonough and Sun, 1995), allowing for easy illustration of U/Pb age and TE composition from zircon rim to core.

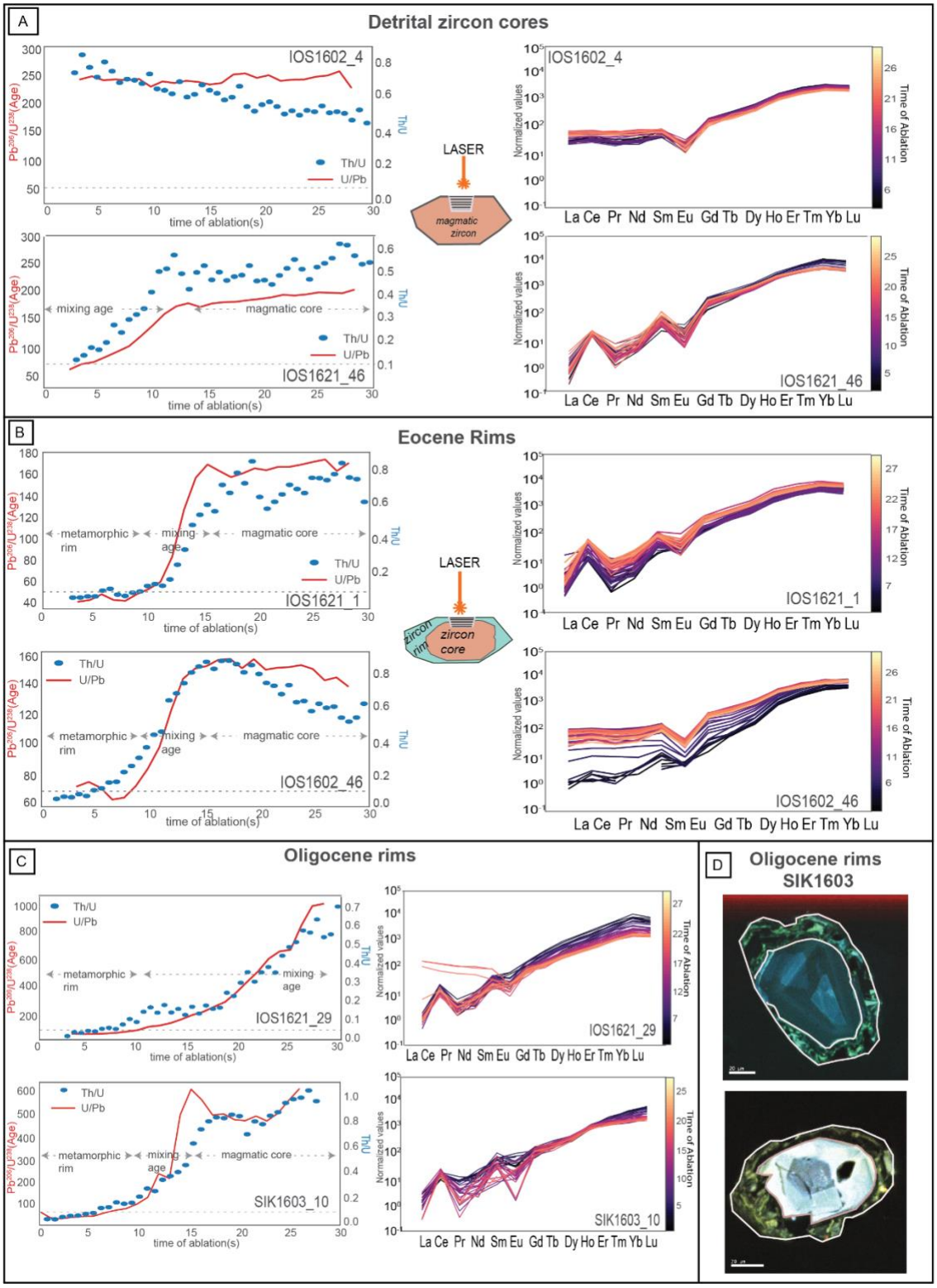

Figure 2: (A, B, C) Split stream depth profile data from different populations of zircon from Ios and Sikinos. Time resolved data are shown in 1 sec increments from 0 sec (rim) to 30 sec (core). Left column: Plots show Th/U (blue dots) and U/Pb Age (red line) vs. time of ablation for individual grains. Age zones are

interpreted as magmatic core, mixing age, or metamorphic rim. The dashed line indicates the Th/U=0.1 indicator of magmatic vs. metamorphic zircon. Right column: Spider diagrams from individual grains normalized to chondrite. Color bar represents the time of ablation exported in 1-sec increments, when rim is present, dark colors represent the rim, lighter colors represent the cores. (A) Examples of detrital zircon cores, bottom grain has a mixing age domain (B) Examples of magmatic cores with Eocene overgrowths (C) Examples of magmatic cores with Oligocene overgrowths. (D) Panchromatic CL images of zircon grains from sample SIK1603.

4.2 Oxygen isotope analyses

Oxygen isotope ratios were measured on apparent core and rim pairs from detrital zircon grains (n = 16) from sample IOS1621 using the CAMECA IMS 1280 high-resolution, multi-collector ion microprobe at the WiscSIMS Laboratory, University of Wisconsin–Madison. Oxygen isotope ratios were analyzed using a $^{133}Cs^{+}$ primary beam focused to a spot of ~10 μm diameter. Analysis pits were 1-2 μm deep. Ions of $^{16}O^{-}$ and $^{18}O^{-}$ were simultaneously collected in two movable Faraday cup detectors with an average $^{16}O^{-}$ intensity of 2.8×10^{9} cps and $^{16}O^{1}H^{-}$ was collected in the axial Faraday cup to check for traces of water in zircon. Cathodoluminescence images were used to identify zircon rims from zircon cores and to guide the placement of the analysis spots. Analytical conditions are described in Kita and Valley (2009), Valley et al. (2009) and Wang et al. (2014). Analyses are calibrated by standard-sample-standard bracketing with four analyses of KIM-5 zircon standard ($\delta^{18}O = 5.09‰$ VSMOW, Vienna Standard Mean Ocean Water; Valley, 2003) before and four analyses after each block of 8 to 14 sample analyses. External precision (reproducibility) is estimated using two standard deviations of the eight analyses of KIM-5 for each sample bracket. The average analytical reproducibility was ±0.19‰ (2σ) on KIM-5 for the brackets of this session. Individual data reported have external precision between 0.17 and 0.20‰ (2σ). Values of $^{16}O^{1}H^{-}/^{16}O^{-}$ (OH/O hereafter) were background corrected for contaminant OH by subtracting the average OH/O values measured on bracketing analyses of KIM-5 zircon standard, that is assumed to be anhydrous (see Wang et al. 2014). Background corrected ratios of OH/O are not calibrated against a standard, but are useful on a relative basis to identify subtle changes in OH content that might indicate radiation damage or hydrous inclusions. All oxygen isotope data including measurements on standards and unknowns are included in Appendix A-DS3.

4.3 Cathodoluminescence imaging and U-Pb maps for zircon (LA-SS)-ICP-MS analysis

For the panchromatic CL imaging, we used FEI Nova NanoSEM 430 field emission SEM and Gatan Chroma CL system at the Bureau of Economic Geology of the University of Texas at Austin. Imaging was performed using 15 kV accelerating voltage, dwell time of 601.5 sec/~10 min/per grain, beam currents of 0.35 nA to a few nA and working distance of 13 mm.

Two-dimensional U-Pb mapping was performed by LA-ICP-MS on 14 polished zircon grains previously analyzed by SIMS for oxygen isotope ratios to delineate the isotopic and elemental concentrations of different zircon zones. Combined with CL images, this method aids in understanding the morphology and growth mechanism of the zircon rim. This technique is especially important when zircon grains preserve very thin rims. To construct U-Pb two-dimensional maps, a grid of closely spaced 5 μm spots is overlaid on a single polished grain. Each spot is ablated for 5 seconds at 5 Hz resulting in pits 2μm deep, preserving an optimal pit width to depth ratio. A typical U-Pb map includes between 150 and 300 spots depending on the zircon size. To minimize motion of the laser stage, blocks of reference materials (GJ1 and Plešovice) were analyzed only at the beginning and end of the run (see Appendix A-DS4). Due to the very short nature of ablation, the ICP-MS method was set to measure only the necessary isotopes ^{206}Pb, ^{207}Pb, ^{232}Th, and ^{238}U. Values for ^{235}U were calculated from the measured ^{238}U using the natural ratio (^{238}U /^{235}U = 137.88). Data reduction was performed using Iolite 3.7 with the VisualAge DRS (Paton et al., 2011; Petrus and Kamber, 2012). Correction for downhole elemental fractionation was minimal due to the very shallow ablation pits. Exported U/Pb age data were combined with coordinate information and a map was created using an in-house Python code. We filtered out ages that have larger than 30% 2-sigma error.

5. RESULTS

We present the results of zircon depth profile U-Pb (42 samples, see Appendix A-DS1) and trace element (three samples, see Appendix A-DS2) analyses from Sikinos and Ios to constrain the timing of metamorphism and the geochemical signature of zircon during these different metamorphic stages. In addition, we present CL images (Fig. S2), SIMS oxygen isotope analyses (one sample, Appendix A-DS3) and two-dimensional zircon elemental maps (two samples, Appendix A-DS4) to further understand grain morphology and the source of the fluids which interacted with these grains during metamorphism.

314 5.1 Zircon U-Pb depth-profiling

315 Of all the samples analyzed previously for U-Pb crystallization and maximum depositional
316 ages (N>100; Flansburg et al., 2019; Poulaki et al., 2019), 42 of them contained zircon with rims
317 that yielded U-Pb ages resolvable by depth-profiling (>1 μm). Zircon rim ages fall into two age
318 groups of ~20 to 35 Ma and ~45 to 65 Ma (Fig. 3). Both metasedimentary and meta-granitoid rock
319 samples from the CBU and CB record Eocene metamorphic rims, whereas only metasedimentary
320 samples in proximity to the CB/CBU contact had additional zircon Oligocene rims. In total, zircon
321 overgrowths were identified in six samples from the CB and 36 samples from the CBU (n = 42,
322 Sikinos=17, Ios=25; Appendix A-Table1).

323 The majority of the CBU samples with Eocene rims (n=34) are quartz mica schists with
324 varying abundance of chlorite, glaucophane, and actinolite, and two samples are meta-
325 conglomerates. Most samples are strongly overprinted with greenschist-facies minerals (e.g.,
326 chlorite, epidote) associated with metamorphic retrogression. Eocene rims preserved within CBU
327 samples constitute up to ~41% of the total zircon grains analyzed within a single sample. Of the
328 six samples collected from the CB which record Eocene age zircon rims, four are granitic gneisses
329 with feldspar, quartz, and white mica, and two are mica schists (Appendix A-Table 1). On Ios,
330 Carboniferous granites and granitic gneisses of the CB also record Eocene metamorphic
331 overgrowths. These samples are located at varying locations in the Ios metamorphic dome and do
332 not correlate to proximity with the CB-CBU contact (Figs. 1 and 3). Eocene rims within plutonic
333 CB samples constitute up to 10% of the total zircon grains analyzed for U-Pb and range in age
334 from ~40 to 65 Ma (Fig. 3) (Flansburg et al., 2019; Poulaki et al., 2019). On Ios, the
335 metasedimentary CB also preserves Eocene rims from 40-60 Ma in <1% of total detrital zircon
336 analyzed.

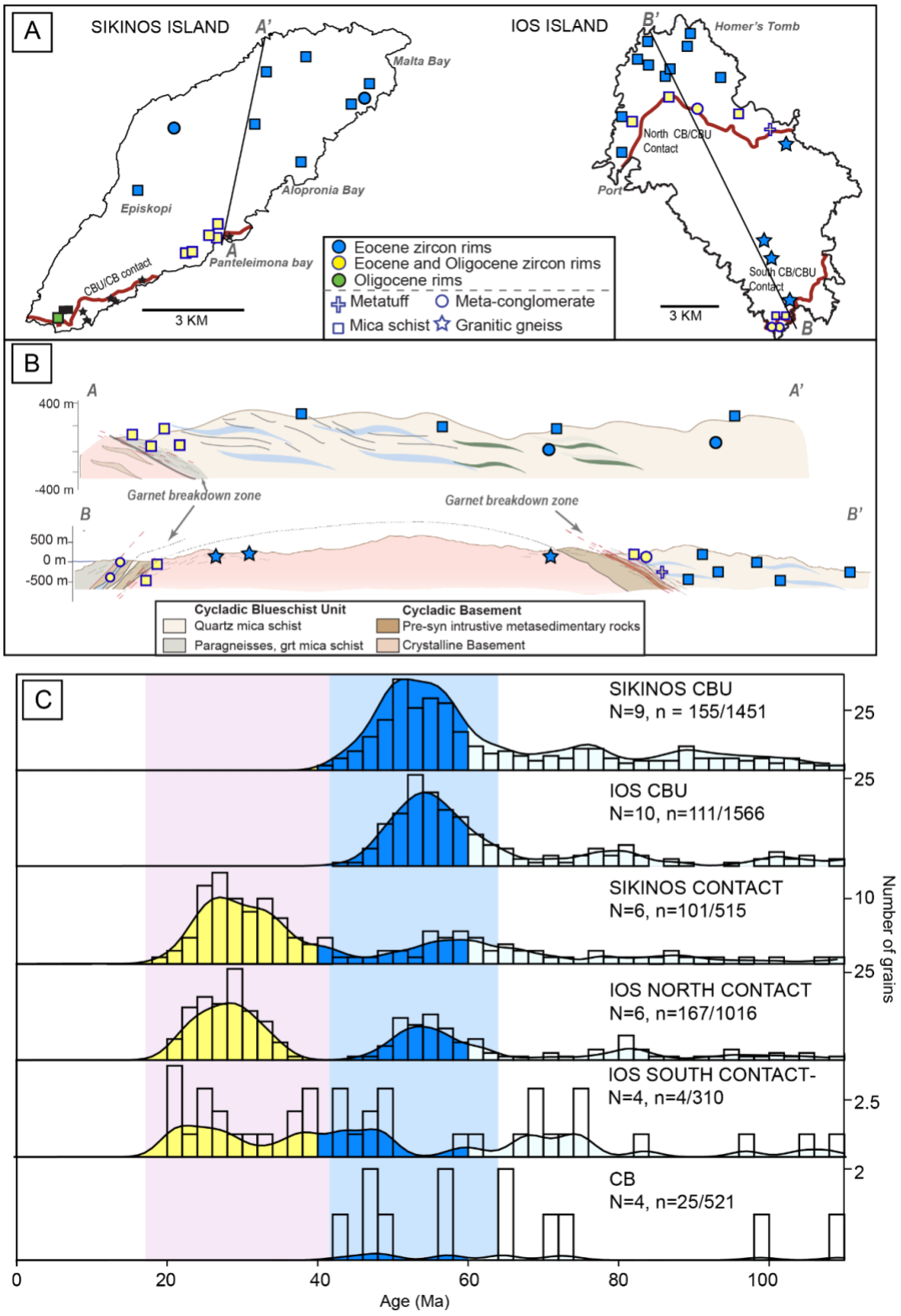

Figure 3: A) Island maps indicate the sample locations and lithologies. B) Cross sections of Sikinos and Ios Islands show relative samples' locations with respect to the CBU/CB contact. C) Metamorphic zircon kernel density estimates (KDEs) of Cycladic Blueschist Unit (CBU) and Cycladic Basement (CB) samples collected from Sikinos and Ios. KDEs represent multiple samples grouped based on the sample location. N

is the number of samples; n is the number of zircon grains. N is the number of samples; n is the number of zircon grains plotted vs. the total number of grains analyzed (grains older than 110 Ma are not shown). Prominent age modes for only the zircon rims are represented by different colors (blue for Eocene, yellow for Oligocene and Eocene).

Thirteen samples collected within 50 m of the CB-CBU contact from both Sikinos (n=7) and Ios (n=6), preserve two different generations of zircon overgrowths at ~20-35 and ~40-65 Ma. Even though zircon rims from the South Contact have the same ages as the other groups they show a wider distribution of ages. This larger spread of data is likely attributed to the smaller number of grains with rims found and analyzed in the samples. Oligocene rims from CBU samples are preserved in up to 44% of the total zircon grains analyzed and the main lithologies are quartz-mica schists with variable amounts of chlorite, albite, sodic amphibole, and garnet with only a few samples containing high pressure indicative minerals (Appendix A-Table 1). Oligocene rims from the metasedimentary CB on Ios were preserved in ~1% of the detrital zircon population. These rims are contained within one conglomeratic garnet-mica schist and one quartz-mica schist collected from the metasedimentary stack on southern Ios west of Magganari, within ~200-500 m of their contact with the intrusive CB granitoids and within 100-200 m of the CBU tectonic sliver (Fig. 1).

The significant dispersion of the observed apparent rim ages is likely attributable to the discordance, inheritance, common lead and high age uncertainties of thin rims. While the use of more restrictive discordance filters narrows the age range of rim growth (Fig. S5), no systematic shift in peak ages is discernible for 30% to 15% discordance filters. The age mode remains the same (Fig. S5) but more discordant rims are excluded. As shown in Figure 4, longer analytical duration (thicker rims) yields more precise and concordant ages that yield an average concordant age for the Eocene rims of 52.7 ± 0.2 and for the Oligocene ages of 25.2 ± 0.1 Ma (Fig. 4). Ages older than ~70 Ma ages will not be discussed in this paper because the youngest MDA of these samples are Late Cretaceous (Poulaki et al., 2019) and it is unlikely that these rims are related to initial subduction metamorphism.

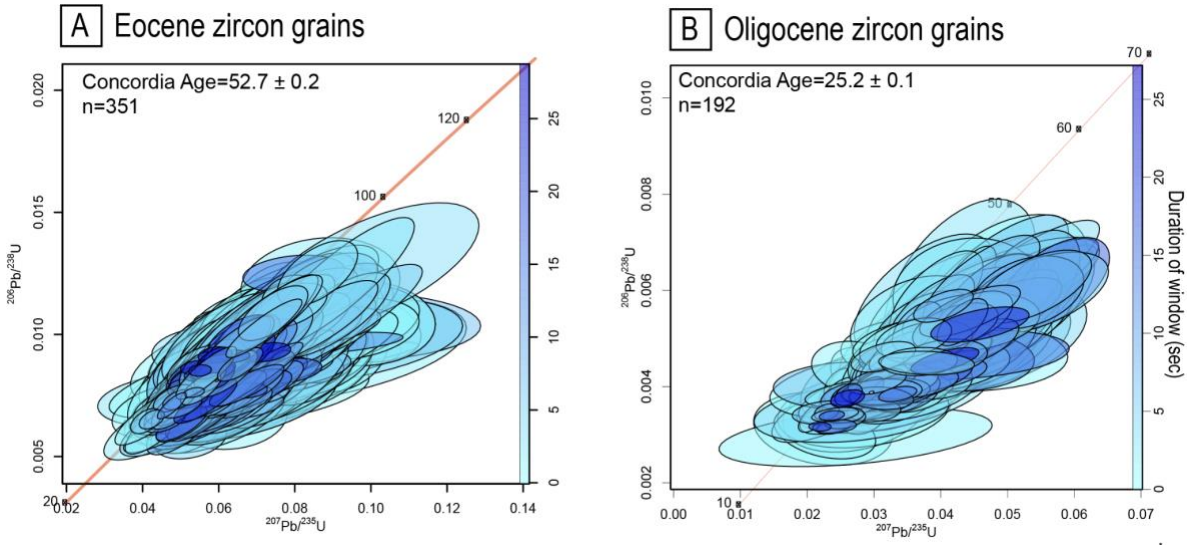

Figure 4: Concordia diagrams for the Eocene (A) and Oligocene (B) zircon grains color-coded by the analytical duration.

5.2 Zircon Split Stream TE and REE compositions

Trace element and REE compositions were analyzed in 46 grains from three samples by (LA-SS)-ICP-MS (Fig. 5, 6, 7, S1). Sample SIK1603 (quartz-mica schist with garnet pseudomorphs, (Fig. 8G-I) preserved only Oligocene rims (n=8 grains); Sample IOS1621 (quartz-mica schist with minor rutile, and minor garnet pseudomorphs) preserved Oligocene and Eocene rims (n=23 grains); Sample IOS1602 (mica-chlorite-feldspar-quartz schist) preserved only Eocene rims (n=15 grains). TE and U-Pb data are time resolved in 1-sec increments of ablation, with ablation time used as a proxy for depth in the grain (from rim to core), and then subdivided into groups of Oligocene rims, Eocene rims, and magmatic cores. Mixing ages between these growth zones were excluded.

Magmatic cores of detrital zircon yield bimodal TE patterns (Fig. 2A). One group of grains (Fig. 2A, grain IOS1602_4) has a strong negative Eu anomaly and lacks a positive Ce anomaly, whereas the second group of grains preserves both a negative Eu anomaly (Fig. 2A- grain IOS1621_46, see Fig. 5F, for Ce/Ce* vs. Eu/Eu*) and a positive Ce anomaly. For all grains, the Th/U ratio is greater than 0.4 and spans up to 2 in the cores (Fig. 5C). REE chondrite-normalized plots do not have very steep profiles for the HREE and MREE (Lu/Sm <1000, Dy/Sm<100, Lu/Ho<10), whereas steeper slopes are observed for some of the samples in the LREE (Nd/La<100) and others preserve flat profiles (Fig. 2A, 5I, L). In the detrital zircon cores, Th

concentrations range from 100 to 2000 ppm and U concentrations range from 0.1 to 2,000 ppm (Fig. 7G-I). Hf concentrations are consistent in the cores among the three samples with values of ~10,000 ppm. Lu and Y concentrations show a large range in the magmatic cores from 10 to 300 ppm and from 500 to 6000 ppm, respectively.

For Eocene zircon overgrowths, calculated Th/U ratios span from 0.05 to 0.4 (Fig. 5B, 6B, C). Chondrite-normalized REE element patterns from individual zircon grain rims and cores show variations in Ce and Eu anomalies both within samples and among grains from the same sample. The Eocene zircon rims, in most cases, have larger Eu and Ce anomalies compared to their corresponding cores (Fig. 6E, F). The Eu anomalies range from 0.1 to 1.0, whereas the Ce anomalies range from 0.1 to 10 for sample IOS1602, and from 6 to 60 for sample IOS1621 (Fig. 5E, 6E, F). The LREE concentrations are depleted within the Eocene rims compared to their cores, the Eocene rims also exhibit less steep slopes with $(Nd/La)_N<25$, than their cores with $(Nd/La)_N<250$ (Fig. 2B, 5K, 6H, I). The measured MREE have similar or lower concentrations within rims and have steeper or similar slopes ($(Dy/Sm)_N<50$), whereas the Eocene rims have flat slopes and are depleted in the MREE in comparison to their cores (Figs. 2B, 5H). The HREE have similar concentrations in both the Eocene rims and the cores $(Lu/Sm)_N<1000$ (Figs. 2B, 5H, 6K, L) with a few outliers in sample IOS1602 with Dy/Sm in the rims being higher than in the cores (Fig. 6K). Th concentrations for the Eocene rim span from 0.1 to 250 ppm (Fig. 7 H, I). U concentrations preserve an opposite pattern with the magmatic cores having concentrations from 100 to 1400 ppm and the zircon overgrowths from 5,000 to 12,000 ppm with three data points at 14,000 (Fig. 7G-I). Hf content is similar to their corresponding core with values ~10,000 ppm, but slightly enriched in some grains of sample IOS1621 with values ~14,000 ppm. A similar pattern is also preserved in the Hf concentrations, with the Eocene rims having the same concentrations as the cores (~10,000 ppm) (Fig. 7A-C). Lu and Y concentrations for the Eocene rims range from 250-300 ppm and 2000-4000 ppm, respectively, and in the same range of values with their corresponding cores (Fig. 7D-F).

The Oligocene rims identified in SIK1603 and IOS1621 exhibit different signatures from both Eocene rims and magmatic cores. The Th/U ratios for Oligocene rims in SIK1603 span from 0.01 to 0.1 and in IOS1621 from 0.05 to 0.3 (Fig. 5A, 6A, C). The Oligocene rims have larger negative Eu anomalies ($Eu/Eu^*<2.5$) with respect to their cores ($Eu/Eu^*<2$), as well as in comparison to the Eu anomalies of Eocene rims ($Eu/Eu^*<1$) in both SIK1603 and IOS1621

samples (Fig. 5D, 6D, F). The Ce anomalies in the Oligocene rims (Ce/Ce*<40) are larger than the anomalies in the Eocene rims (Ce/Ce*<30) for sample IOS1621 and similar for sample SIK1603. Ce is overall depleted for the Oligocene rims in comparison to their corresponding cores Ce/Ce*<100 for sample SIK1603 and has similar concentrations in sample IOS1621 (Fig. 5D, F, 6D, F). The MREE and HREE in the Oligocene rims are highly enriched (Fig. 2C) with steep slopes ($(Lu/Sm)_N$<2000) in comparison to both the depleted cores with flat slopes ($(Lu/Sm)_N$<500) and the Eocene rims ($(Lu/Sm)_N$<1000) (Fig. 5C, G, 6J, L). The HREE are also highly enriched in the Oligocene zircon rims in comparison to their cores. Oligocene rims in sample SIK1603 have steep slopes ($(Lu/Ho)_N$<50 with respect to their cores ($(Lu/Ho)_N$<10, while IOS1621 has flatter slopes ($(Lu/Ho)_N$<15 with respect to cores that have ($(Lu/Ho)_N$ <6 (Fig. 5C, J, 6G, I). The LREE of Oligocene rims are depleted with respect to their cores and have less steep slopes ($(Nd/La)_N$<30, with two data points with ($(Nd/La)_N$=120) in contrast to the magmatic cores ($(Nd/La)_N$ <250), similar to the depletion evident in Eocene rims when compared to their corresponding cores (Fig. 5C, J, 6G-I). For sample SIK1603, Th concentrations span from 0.01 to 50 ppm, while Oligocene rims in both samples have lower Th concentrations than their cores. The U concentrations preserve an opposite pattern with concentrations from 0.1 to 10,000 ppm, with the lower values present in sample SIK1603 (Fig. 7G-I). The Hf contents of Oligocene rims are enriched in both samples (Hf =6,000-16,000 ppm) in comparison to their cores and Eocene rims (Fig. 7A-C). Y concentrations in sample SIK1603 are similar between rims and cores with ~500 to 1000 ppm, whereas in sample IOS1621 the rims have similar or slightly higher concentrations of Y than the cores at ~4000 to 7000 ppm. Lu is enriched in both samples with values from 100 to 600 ppm (Fig. 7A-F).

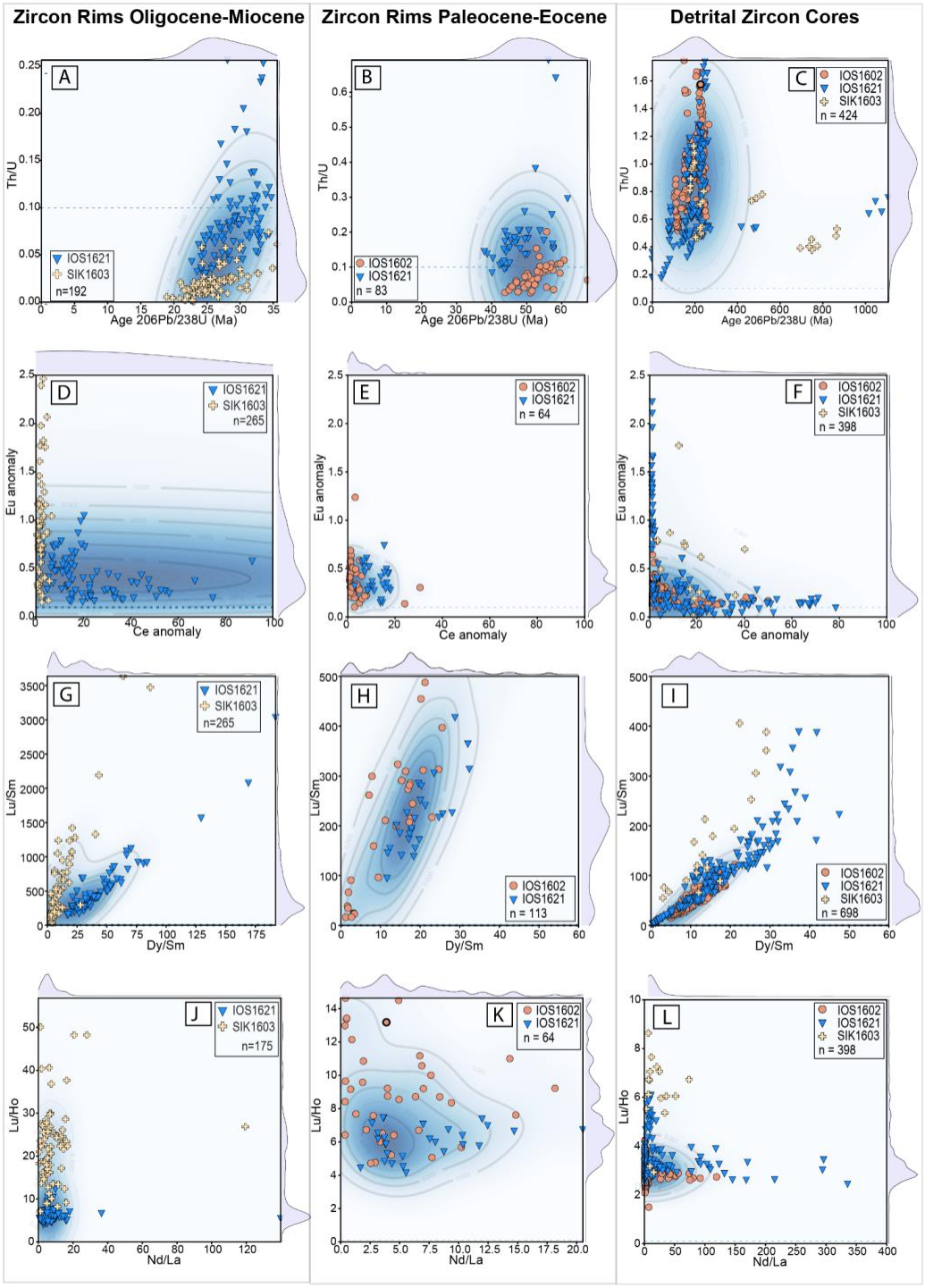

Figure 5: Split stream data exported in 1-sec increments and categorized based on the age: Oligocene, Eocene or older magmatic cores, labels indicate the sample number, mixing ages are excluded. Note that the scale changes on each plot. (A-C) Th/U vs. $^{206}Pb/^{238}U$ final age (Ma) discrimination line at Th/U= 0.1 (D-F) Eu/Eu vs. Ce/Ce* (G-I) Lu/Sm (HREE/MREE) normalized to chondrite vs. Dy/Sm (MREE) normalized to chondrite (J-L) Lu/Ho (HREE) normalized to chondrite vs. Nd/La (LREE) normalized to chondrite.*

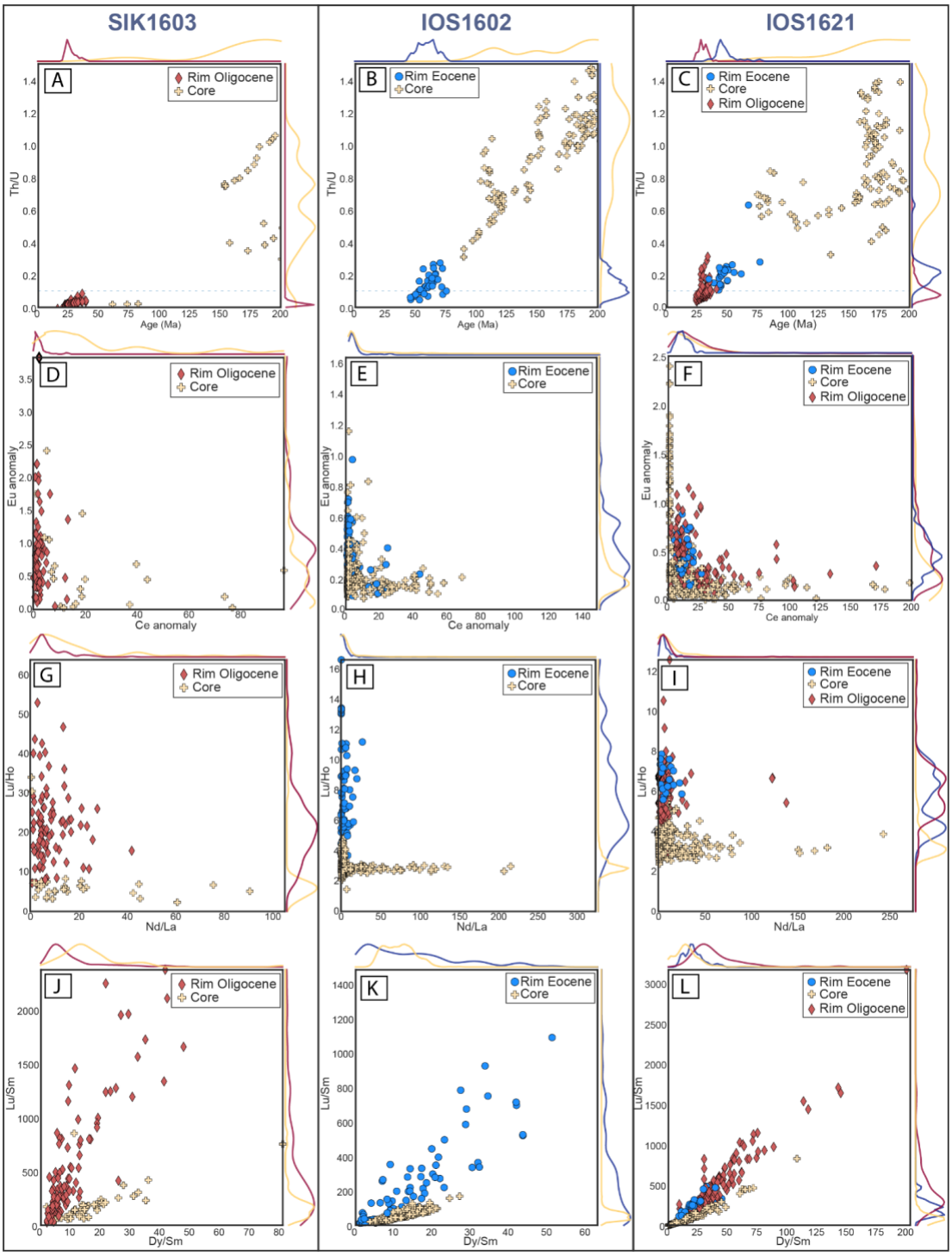

Figure 6: Split stream data exported in 1-sec increments and grouped based on the sample and labeled based on the age, mixing ages are excluded. (A-C) Th/U vs. $^{206}Pb/^{238}U$ final age (Ma) discrimination line at Th/U= 0.1 (D-F) Eu/Eu vs. Ce/Ce* (G-I) Lu/Sm (HREE/MREE) normalized to chondrite vs. Dy/Sm (MREE) normalized to chondrite (J-L) Lu/Ho (HREE) normalized to chondrite vs. Nd/La (LREE) normalized to chondrite.*

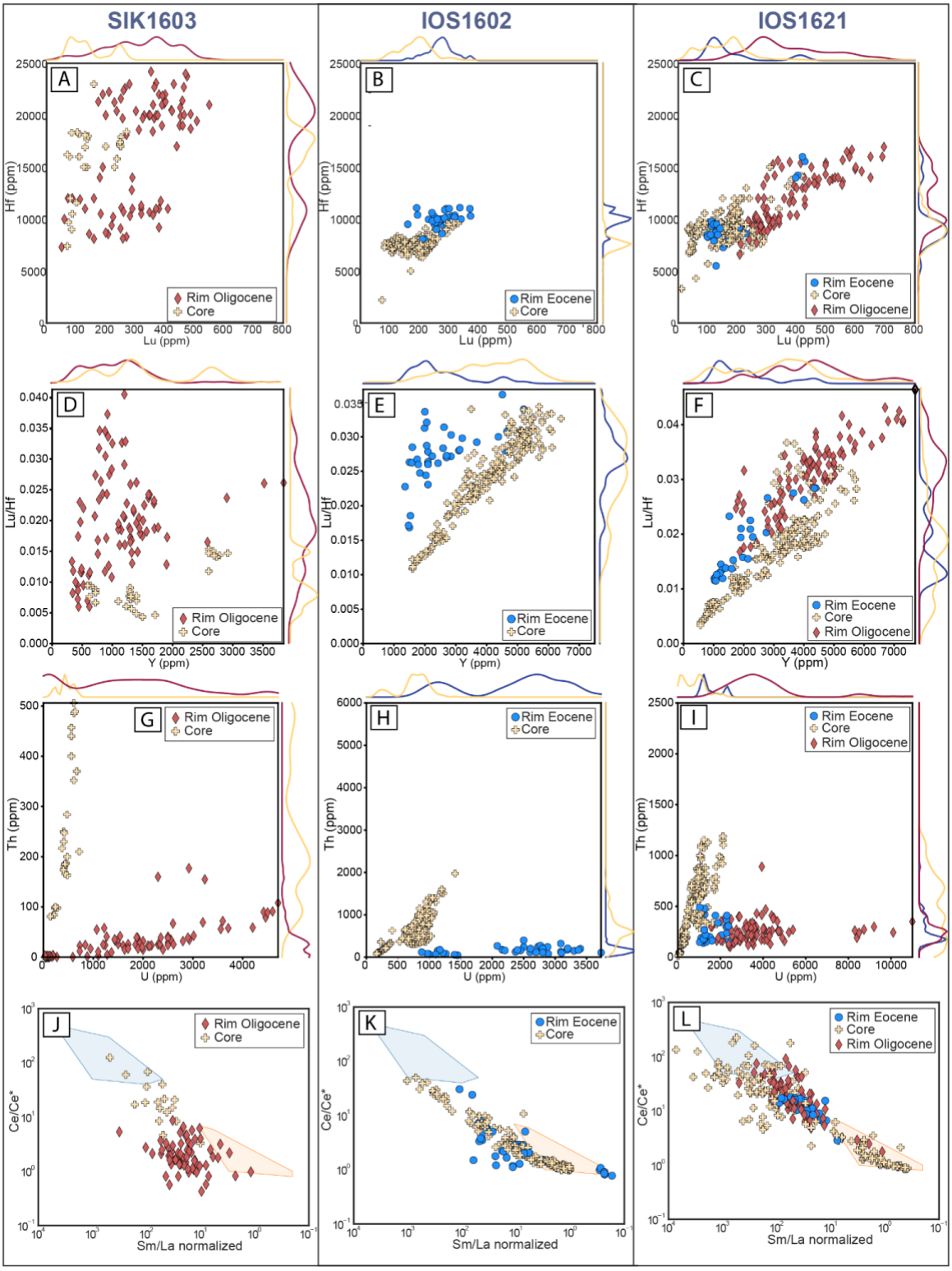

457

458 *Figure 7: Split stream data exported in 1-sec increments and grouped based on the sample and labeled*
459 *based on the age, mixing ages are excluded. (A-C) Hf (ppm) vs. Y(ppm) (D-F): Lu/Hf vs. Y(ppm) (G-I) U*
460 *vs. Th (ppm) (J-L) Plots from Hoskin (2005) with discrimination fields for magmatic (blue) and*
461 *hydrothermal zircon (orange). Note that the scale changes on each plot.*

462 5.3 Cathodoluminescence and two-dimensional U-Pb age maps

463 Panchromatic CL images were taken of 18 zircon grains from sample SIK1603 and
464 IOS1621 that preserved Oligocene overgrowths, and monochromatic CL images were made for
465 12 zircon from sample IOS1621 that preserve Eocene and Oligocene overgrowths (Fig. S2). The
466 CL images show distinct rims that transect primary textures (Figs. 2D, 9, 10, S2). The
467 panchromatic CL images of the Oligocene rims (Figs. 2D, S2) reveal strong color differences
468 among different zones, with most of the grains preserving two or three distinct zones. In most
469 grains, a uniform dark core is surrounded by a well-developed inner zone, whereas the outermost
470 zones have lighter spectra as well as a "cauliflower" texture (Figs. 2D, S2). The zircon grains with
471 Eocene rims are mostly euhedral and have magmatic cores with oscillatory zoning (Fig. 9). The
472 Eocene rims do not have zoning and are homogeneous in the CL images.

473 Spatial age variations within these zircon grains were further investigated by obtaining U-
474 Pb maps of 14 grains to understand the 2-D heterogeneity of elements and the U-Pb age
475 distributions within these zircon, confirming the results of the depth profile analyses (Appendix
476 A-DS4). The cauliflower-spongy texture shown in CL imagery correlates uniquely to rims with
477 Oligocene ages, whereas the cores vary in age (250 to 1200 Ma). These two-dimensional U-Pb age
478 maps further reveal that rims consistently have high U concentrations (1800 to 3000 ppm) and low
479 Th concentrations (10 to 307 ppm), contributing to a Th/U < 0.1 (Figs. 9 and 10). For these maps,
480 we used the pixels with statistically equivalent dates, including data within the 95% of the Gaussian
481 distribution, to eliminate anomalously young and mixed ages to calculate the mean ages and
482 uncertainties shown in the maps. The ages of interpolated pixels within the Oligocene aged rims
483 spread from 22-32 Ma with mean age at 27.1 ± 3.4 Ma while the individual pixels within the
484 Eocene-aged rims span from 32 to 65 Ma with mean age at 46.8 ± 7.6 Ma (Fig. 9, 10). The ages
485 of the detrital cores span from ~300 Ma to ~1 Ga.

486 5.4 Oxygen isotope geochemistry

487 Detrital zircon cores from sample IOS1621 have $\delta^{18}O$ values ranging from +5.6 to +8.5‰
488 (Figs. 9, 10, Appendix A-DS3). Zircon rims yield $\delta^{18}O$ values ranging from +6.9 to +8.9‰. Of the
489 16 grains analyzed, five have zircon rims with $\delta^{18}O$ values up to 1.6‰ higher than their respective
490 zircon cores, with one rim exhibiting a 3.3‰ increase (Fig. 10A). Conversely, four grains have
491 zircon rims with $\delta^{18}O$ values lower relative to their cores (with one rim 1.8‰ lower). Given an
492 analytical precision of ±0.2‰ (2 SD) on each analysis, the rim-core pairs for the zircon with

Eocene age rims are essentially statistically indistinguishable with $\delta^{18}O$ differences of $\leq 0.5‰$. However, in zircon with Oligocene age rims, three of the rim-core pairs record $\delta^{18}O$ differences of $\geq 1‰$. SIMS analysis from two Eocene-aged rims (grain 5, 9, Appendix A-DS3) straddles the core-rim boundary according to the CL image, therefore the reported $\delta^{18}O$ value of the rim represents a mixture of the zircon core and rim and is excluded from further interpretation; although the true $\delta^{18}O$ value of this rim remains unknown, the data suggest the Eocene rim for this grain is more depleted in ^{18}O relative to the zircon core.

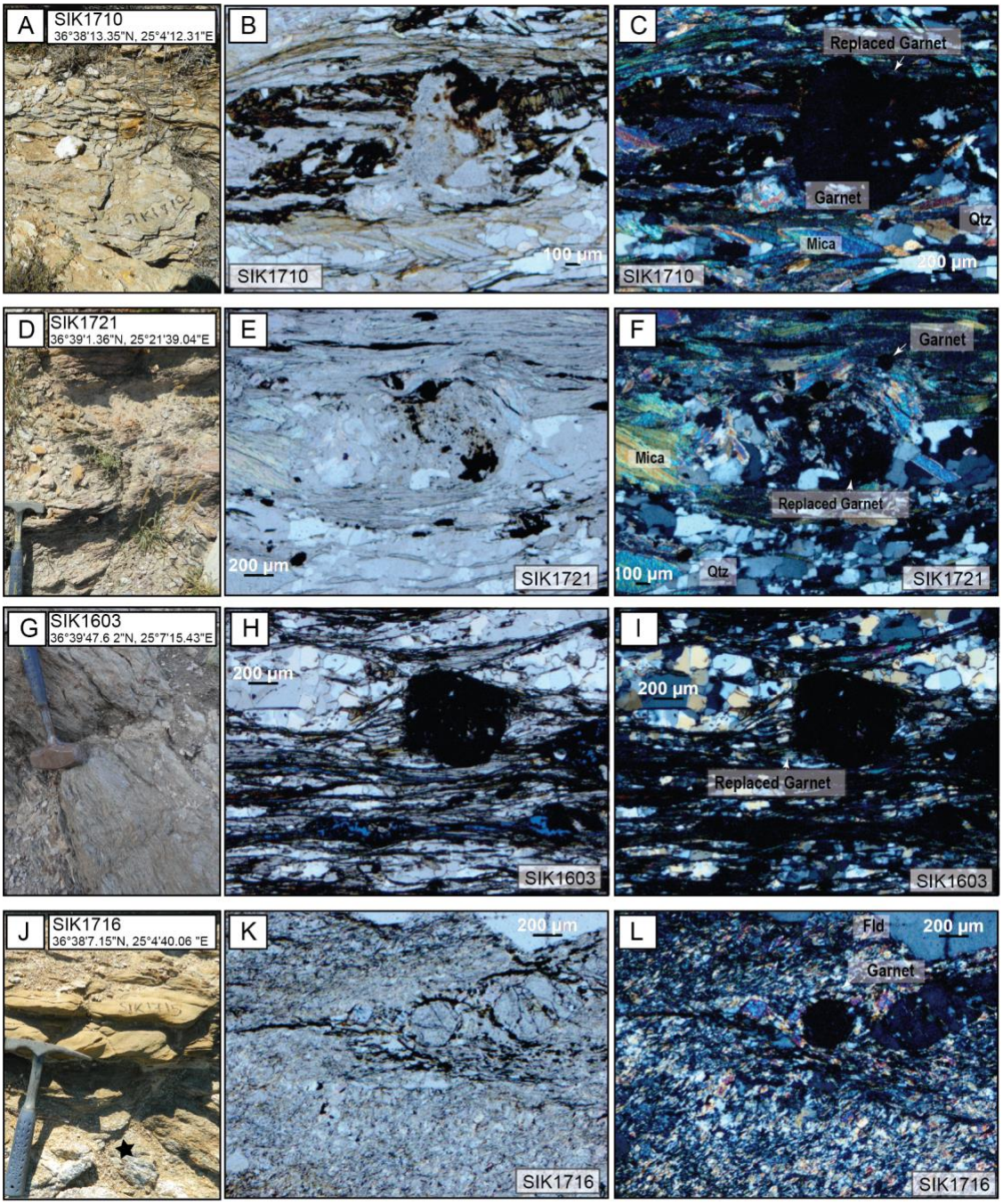

Figure 8: First column shows macroscopic pictures of samples in the field, second and third column shows microscopic pictures of the samples shown on the left. (A-C) sample SIK1710 collected along the CB/CBU contact (D-F) sample SIK1721 collected along the CB/CBU contact (G-I) sample SIK1603 collected along the CB/CBU contact (J-L) sample SIK1716 collected from the SE part of the Sikinos Basement. Orthogneiss with pristine garnet.

6. DISCUSSION

Samples were collected from Sikinos and Ios from both the Cretaceous to Permian metasedimentary CBU and the metasedimentary rocks and metagranitoids of the Carboniferous

and older CB. Previous work on these islands (Poulaki et al., 2019, Flansburg et al. 2019) established the detrital MDA from Permian to Cretaceous and crystallization ages of CB (Carboniferous) and CBU protoliths (Triassic metatuffs) (n=120). From this sample suite, a subset of samples was analyzed to constrain the Cenozoic metamorphic and metasomatic evolution of these rocks. The detrital zircon age spectra of the CBU rocks span from ~70 Ma to ~3 Ga with the youngest MDA of ~70 Ma (Flansburg et al., 2019; Poulaki et al., 2019). The CB comprises Carboniferous granitic gneisses hosted within a suite of Neoproterozoic to early-Carboniferous metasedimentary rocks (Flansburg et al., 2019, Zlatkin et al., 2018). This study shows that together, both the CB and CBU represent an exhumed subduction complex that experienced at least two tectono-metamorphic events in the Eocene (HP/LT) and Oligocene (greenschist phases (e.g., Baldwin and Lister, 1998; Forster et al., 2020)). Zircon U-Pb and TE depth profiling and U-Pb two-dimensional mapping presented in this study show that these Mesozoic and Paleozoic zircon grains exhibit two distinct phases of Cenozoic metamorphic overgrowths coincident with these events (Fig. 3). Based on the youngest MDAs and the geologic setting of the Hellenic subduction zone, it is evident that these overgrowths are related to subduction-related metamorphism. The grains with ages older than the MDAs are not the focus of this study and will not be further discussed.

6.1 Zircon rims and relation to regional metamorphism

Mean Eocene concordant zircon rim ages (52.7 ± 0.2 Ma) from this study are in excellent agreement with the timing of HP/LT Eocene subduction metamorphism constrained by various studies (Baldwin, 1998; Bröcker et al., 1993; Bröcker and Franz, 1998; Dragovic et al., 2015; Lagos et al., 2007; Lister and Forster, 2016; Schneider et al., 2011; Tomaschek et al., 2003). Thus, we suggest that the Eocene zircon rims reflect growth either during, shortly after, or before the peak of the HP/LT conditions, and hence their geochemical signatures can be tied directly to well-studied metamorphic conditions within the Hellenic subduction zone (Andriessen et al., 1979; Baldwin, 1996; Bröcker et al., 1993; Dragovic et al., 2015; Lagos et al., 2007; Lister and Forster, 2016; Tomaschek et al., 2003; Wijbrans and McDougall, 1986, 1988). Rims with overlapping analytical uncertainties are observed in both the CB and the CBU (this study; Flansburg et al., 2019), consistent with both units being subducted and experiencing subduction-related metamorphism at the same time. There is no obvious correlation between metasedimentary MDAs (tectono-stratigraphy) and the Eocene metamorphic rims (Poulaki et al., 2019). The lithologies that

preserve metamorphic overgrowths include quartz-mica schists and orthogneiss with various amounts of chlorite, albite, calcite, glaucophane, garnet, actinolite, and feldspar (Appendix A-Table 1). In contrast to the CBU, only five out of fifty samples from the CB preserved Eocene metamorphic rims and their lithologies include granitic gneisses and garnet-mica schist. The zircon grains with Eocene rims lack regular growth textures and have detrital cores with oscillatory zoning and the rims are separated from cores by irregular contacts and do not show any zoning (Fig. 9, S3).

The mean concordant Oligocene zircon rim ages (25.2 ± 0.1 Ma) overlap with the proposed timing of retrograde metamorphism documented in the Cyclades such as on Syros and Naxos, with ages range from ~19 to ~27 Ma (Andriessen et al., 1987, 1979, 1991; Duchêne et al. 2006; Miller et al., 2009; Wijbrans and McDougall 1988). Notably, data from this study show that on Sikinos and Ios, these rims are only found in samples collected along and within ~100 m of the CB-CBU contact. Only metasedimentary samples have the Oligocene rims and their lithologies are limited to quartz-mica schists with minor epidote. A later greenschist overprint completely replaces garnet with chlorite (Fig. 8A-I). Sample SIK1721 (Fig. 8E, F) preserves some garnet near the garnet pseudomorphs. Samples further away from the contact, which do not have Oligocene rims, contain unaltered garnet (Fig. 8J-K).

The structural morphology of the Oligocene zircon rims also provides information about the processes of rim formation. CL images from samples SIK1603 and IOS1621 show that these rims share sharp boundaries with the pre-existing magmatic zoning within the zircon and preserve a spongy/cauliflower texture (Fig. 10, S2), which likely indicate that these rims formed within melt- or fluid-rich systems and grew from precipitation of a fluid (e.g., Geisler et al., 2017). U-Pb maps further support the depth-profile results, showing thin Oligocene ~25 Ma rims that preserve a sharp contact with older magmatic cores.

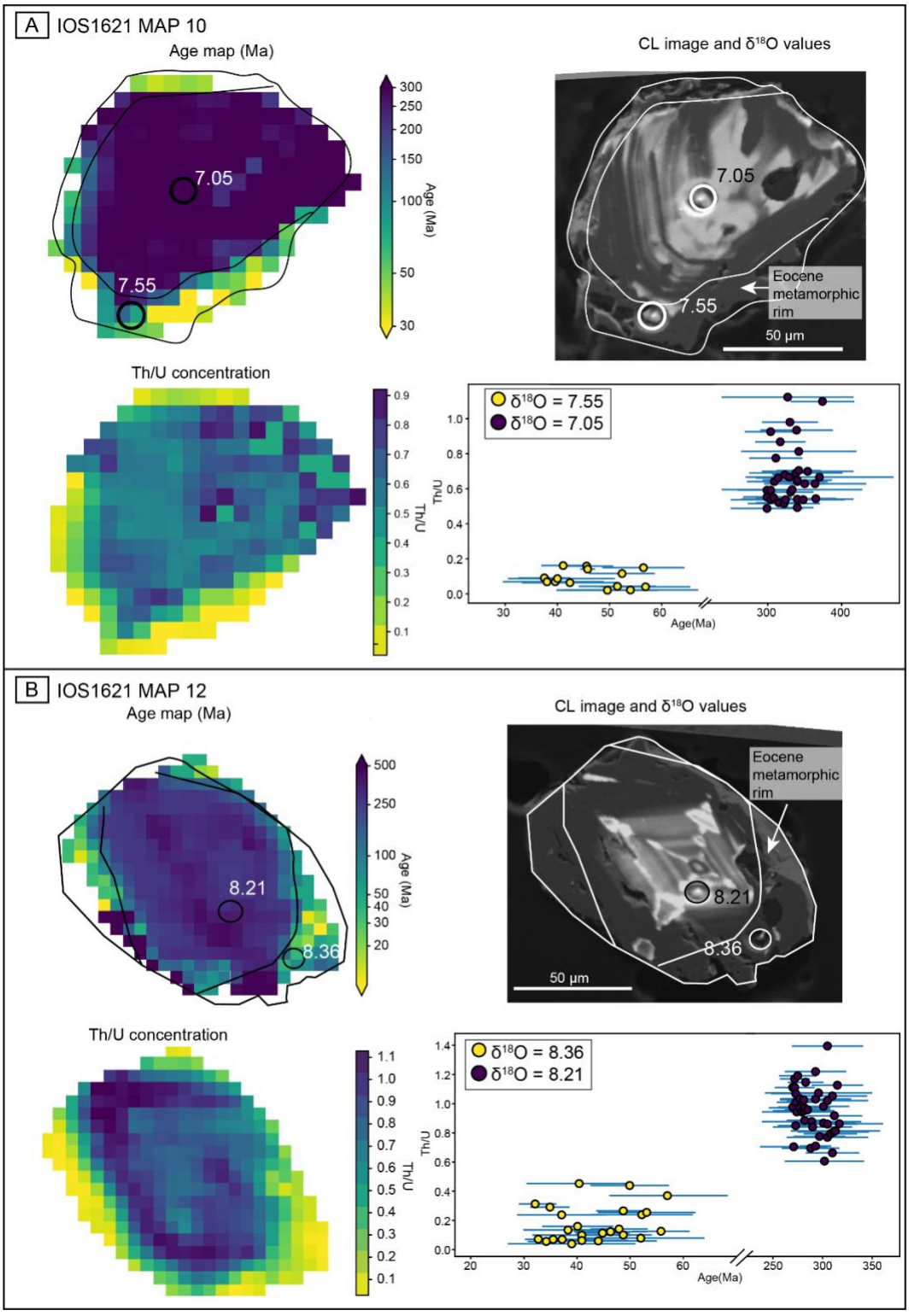

Figure 9: Eocene zircon grains from sample IOS1621. On the right: Two-dimensional maps showing $^{238}U/^{206}Pb$ age (non-linear colorbar) and Th/U values (linear colorbar). On the left: CL images are overlain on secondary electron images to show zonation apparent in the CL image and the corresponding zircon topography of the polished surface of the corresponding zircon, and x-y plot showing Th/U Vs Age and the $\delta^{18}O$ value for the rim and the core. Errors in ages are in 2sigma.

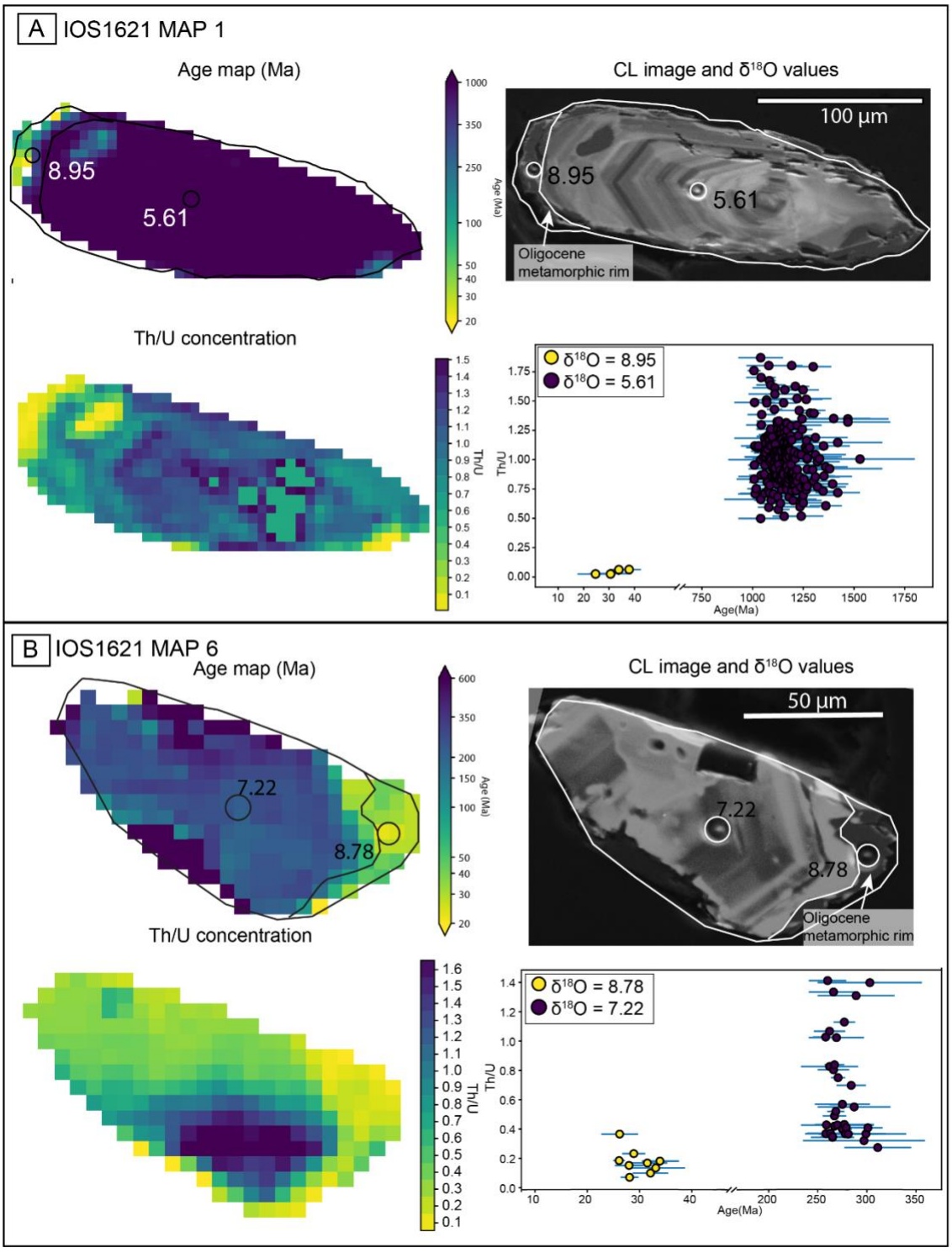

571

572 *Figure 10: Oligocene zircon grains from sample IOS1621. On the right: 2D elemental maps showing*
573 *$^{238}U/^{206}Pb$ age (non-linear colorbar) and Th/U values (linear colorbar). On the left: CL images are overlain*
574 *on secondary electron images to show zonation apparent in the CL image and the corresponding zircon*
575 *topography of the polished surface of the corresponding zircon, and x-y plot showing Th/U Vs Age and the*
576 *$\delta^{18}O$ value for the rim and the core. Errors in ages are in 2sigma.*

577 6.2 Metamorphic zircon geochemistry

578 6.2.1 Trace Elements and REE for the Eocene and Oligocene aged rims

579 The zircon samples with Eocene rims preserve cores with Th/U ratios of 0.3 to 2.0,
580 suggesting a magmatic origin for the detrital cores (Fig. 5A, B). In contrast, the Eocene rims have
581 lower Th/U (0.05 to 0.3), compared to the cores. As with the Eocene rims, the Oligocene zircon
582 rims also record lower Th/U compared to the cores. The Th/U values of the Oligocene zircon
583 overgrowths are all < 0.1, averaging to 0.05, compared to the cores with values of 0.4 to 0.8. In
584 addition, the Oligocene zircon rims have lower Th/U values than the Eocene rims. A value of Th/U
585 < 0.1 is the proposed delineation for the discrimination between magmatic and
586 metamorphic/hydrothermal zircon (e.g., Rubatto, 2007). Even though this boundary value has been
587 suggested as overly simplistic as other factors can influence this ratio, such as pre-existing zircon
588 and/or the presence of monazite (e.g., Hoskin and Black, 2000; Möller et al., 2002, 2003; Pidgeon,
589 1992; Yakymchuk et al., 2018), our data are consistent with the proposed values for metamorphic
590 rims and magmatic cores.

591 The Oligocene rims have higher Hf concentrations than their cores, whereas the Eocene
592 rims have the same or slightly enriched Hf concentrations as their corresponding cores. Previous
593 studies show that the Hf concentrations in metamorphic rims are similar to the magmatic cores
594 (Hoskin and Black, 2000; Kinny and Maas, 2003; Rubatto, 2002). Although low Lu/Hf ratios are
595 indicative of metamorphic zircon (Zheng et al., 2005), the Oligocene grains do not follow this
596 pattern due to enrichment of Lu in the rims. In contrast to both the high Lu/Hf Oligocene rims, the
597 Eocene rims have the same ratio as their corresponding cores suggesting that they are likely
598 comprised of recycled material from the magmatic zircon (Fig. 7D-F).

599 Some of the rims record negative Eu and positive Ce anomalies. These results are
600 consistent with previous observations from HP/LT Eocene recrystallized zircon in the Cyclades
601 (Schneider et al., 2011; Tomaschek et al., 2003). For example, Eocene metamorphic zircon from
602 Serifos island record an overall depletion in MREE and HREE, while still preserving negative Eu
603 and positive Ce anomalies. These studies proposed that the main mechanism of zircon
604 recrystallization is dissolution-reprecipitation (Schneider et al., 2011; Tomaschek et al., 2003) and
605 that the newly formed metamorphic zircon can no longer incorporate REE as it does under
606 metamorphic conditions and therefore will be depleted in REE (Putnis, 2002; Tomaschek et al.,

607 that 2003). Even though the negative Eu and positive Ce anomalies are pronounced, the LREE
608 present are overall depleted and have a flat pattern (Fig. 2B, 5K).

609 Elevated values of La (low Sm/La) and flat LREE are prominent in some of the zircon
610 cores from samples IOS1602 (Fig. 2B) and IOS1621 (Fig. S2). Low Sm/La has been proposed as
611 diagnostic for hydrothermal zircon (Hoskin, 2005), whereas Cavosie et al. (2006) distinguished
612 zircon grains with flat LREE profiles as "Type-2" characterized by high Th/U and discordant U-
613 Pb ages and interpreted as radiation damaged and altered igneous zircons. Alternatively, Type-2
614 zircon could also be the result of inclusions. However, the flat LREE cores of zircon grains in
615 samples IOS1602 and IOS1621 yielded concordant U-Pb ages with low Th/U suggesting a
616 metamorphic or hydrothermal origin.

617 The zircon with Oligocene rims are enriched in HREE relative to their cores (Fig. 2C). The
618 enriched HREE patterns in the Oligocene rims contrast with the overall depleted and flat HREE
619 patterns of the HP/LT Eocene zircon rims (Fig. 2B, C). Despite consistency in HREE, the LREE
620 in the Oligocene rims are more variable, displaying variable degrees of enrichment and depletion
621 in comparison to their cores (Fig. 2C). Overall, LREE and MREE in Eocene zircon rims are more
622 depleted than, or have similar concentrations to, their cores (e.g., IOS1621_1 Fig. 2B, S1), or
623 significantly depleted LREE in the rims with flat LREE in their cores (e.g., IOS1602_46, Fig. 2B).
624 Additionally, some grains have slightly enriched HREE and depleted M-LREE in their rims (e.g.,
625 IOS1602_25, Fig. S1). Conversely, the TE and REE from the Oligocene rims show large variations
626 in their concentrations and they are highly enriched from their corresponding cores.

627 6.2.2 Oxygen isotope composition of zircon core and rim pairs

628 The $\delta^{18}O$ values (+5.6 to +8.5‰) of the zircon cores are consistent with crystallization
629 from magmas that experienced some degree of crustal contamination. Zircon in equilibrium with
630 the mantle have $\delta^{18}O$ values of +5.3 ± 0.6‰ (2SD, Valley, 2003), whereas crust is enriched in ^{18}O.
631 Data presented here are consistent with the $\delta^{18}O$ values of Triassic and Cretaceous detrital zircon
632 cores from the Cyclades (Syros, Tinos, Andros, Ios, Sifnos, Naxos), which have $\delta^{18}O$ values
633 between 2.7 and 10.1‰, with a majority of values falling between 4.7 and 5.5‰ (Martin et al.,
634 2006; Fu et al., 2012, 2015); and are interpreted to originate in an arc-setting that assimilated
635 continental crust (Fu et al., 2010 2012, 2015). The broad age range (~300 Ma to ~1.5 Ga) of the
636 zircon cores from Ios (Fig. 9, 10, Appendix A-DS3) are typical of the passive margin sediments

637 of the CBU (e.g., Poulaki et al., 2019, Seman et al., 2017). These age data combined with magmatic
638 $\delta^{18}O$ values provide additional support for their proposed detrital origin.

639 The Eocene zircon rims (n=3) with ages from ~34 to ~49 Ma have $\delta^{18}O$ values from 6.9 to
640 8.8‰ (average = 7.9‰ ± 0.8‰). Eocene rims are both enriched and depleted in ^{18}O relative to
641 their cores ($\delta^{18}O_{rim\text{-}core}$ = -0.2 to +0.5‰), which have $\delta^{18}O$ values between +7.1 and 8.5‰ (Fig. 9,
642 Appendix A-DS3). The limited difference between the rim and core pairs from the same zircon
643 can be explained by analytical uncertainty (±0.2‰) and/or slight changes in temperature or bulk
644 composition. The low degree of oxygen isotope ratio variability does not require an external fluid
645 source and does not suggest large changes in the temperatures of formation.

646 Alternatively, the Oligocene rims (n=4) have $\delta^{18}O$ values between 8.6 and 9.0 ‰, with an
647 average of 8.8 ± 0.3 ‰ (2SD) and are consistently higher than the $\delta^{18}O$ values of the Eocene rims.
648 All the Oligocene rims are enriched in ^{18}O relative to their cores ($\delta^{18}O_{rim\text{-}core}$ = +0.4 to +3.3‰)
649 (Appendix A-DS3). Shifts in $\delta^{18}O$ values greater than 1‰ are commonly interpreted as involving
650 an externally derived fluid (e.g., Kohn and Kelly, 2018), however, they do not necessarily require
651 an externally derived fluid and can also be explained by changes in temperature and/or assemblage
652 (e.g., Rubatto, 2017). The CBU and CB have experienced Eocene blueschist metamorphism with
653 peak temperature in range from 470 to 540°C (Augier et al., 2015; Gupta and Bickle, 2004; Huet
654 et al., 2009; Perraki and Mposkos, 2001). The Oligocene rims were formed during greenschist
655 facies with peak temperature estimates calculated on Tinos as low as ~400°C (Bröcker et al., 1993).
656 These temperatures suggest a maximum possible temperature difference of 140°C at the time of
657 zircon rim growth. If we assume a maximum possible temperature shift of ~140°C and zircon
658 equilibrium with quartz in a pure quartzite, then the $\delta^{18}O$ value of the zircon would shift by 1.8‰
659 (Valley, 2003). However, zircon-quartz fractionation in quartzite represents an extreme scenario,
660 as the samples also contain plagioclase, mica, ± garnet, and ± trace amounts of rutile, all of which
661 would result in lower fractionations (Valley, 2003). Therefore, we suggest that ^{18}O enrichments
662 greater than ~1‰ are likely due to the influence of an externally derived fluid source, in agreement
663 with findings for rocks of similar mineralogies and P-T paths as reported by Vho et al. (2020). In
664 all cases, the Oligocene rims have $\delta^{18}O$ values higher than the associated cores, reflecting an ^{18}O-
665 enriched fluid likely from a sedimentary derived source (e.g., Sharp, 2007 and references therein).
666 On Naxos, Martin et al., (2006) found three generations of rims: Two Eocene populations at 55
667 and 45 Ma related to HP metamorphism with $\delta^{18}O$ values in the rims similar to the cores, and a

668 third generation at 16 Ma related to low $\delta^{18}O$ fluids and medium temperatures. Future work on
669 oxygen isotope analyses on other Cycladic islands can further evaluate this hypothesis.

670 6.3 The Metamorphic conditions of zircon rims formation

671 6.3.1 Eocene high-pressure zircon metamorphic rims represent recrystallization of magmatic cores

672 Eocene zircon rims are observed in both metasedimentary and meta-granitoid lithologies
673 from the CBU and CB, although they are more widespread in the CBU, suggesting a limited
674 protolith influence on the formation of zircon overgrowths. Although these Eocene zircon rims are
675 metamorphic in origin and related to regionally well-documented HP/LT metamorphism, they
676 exhibit variable TE signatures spanning both the magmatic and hydrothermal fields defined by
677 Hoskin (2005) (Figs. 2B, 5E, H, K, 7). This TE variability is likely attributable to a combination
678 of limited neo-growth from local metamorphic reactions and recrystallization of magmatic zircon
679 cores, resulting in inherited magmatic TE signatures. The similar H-MREE in the Eocene
680 metamorphic zircon rims suggest geochemical inheritance of immobile REE from the
681 recrystallizing zircon cores. Depletion of LREE could also be explained by mica growth along the
682 prograde metamorphic path. Formation of thin Eocene zircon rims is ultimately controlled by P-T
683 conditions and the presence of pre-existing zircon, with host-rock lithology playing a minor role.

684 The variability of REE data from zircon rims grown (Fig. 2, 5, 6, 7) in the same
685 metamorphic conditions and within the same sample likely reflect a) both local protolith
686 heterogeneity and short diffusion length scales, resulting in variable REE availability in the
687 subduction zone system (Kohn and Kelly, 2018) and b) possible disequilibrium conditions at these
688 moderate HP/LT conditions, and c) the lack of minerals that dominate the HREE budget, such as
689 garnet. However, the Th/U of these Eocene zircon rims are lower (0.3 to 0.05) than values typical
690 of magmatic zircon, as well as their corresponding detrital cores (Fig. 5A, B). More importantly,
691 the Th/U of these rims is relatively consistent despite the widely-varying REE signatures. This
692 observation suggests Th/U is more diagnostic of the metamorphic origin, and that Th and U are
693 more strongly fractionated by accessory minerals like allanite and/or monazite that dominate the
694 U and Th budget.

695 Although overall REE depletion of Eocene rims indicate a metamorphic origin for these
696 zircon overgrowths (Rubatto and Hermann, 2007), the magnitude of the MREE and LREE
697 depletion, the slight enrichment of HREE and the existence of Eu and Ce anomalies are atypical

of metamorphic zircon and typical of magmatic zircon. The overall depletion of the Eocene rims reflects the fluid immobility of HFSE elements during HP/LT metamorphism. This contrast is likely related to the lower grade of metamorphism compared to those of Rubatto and Hermann (2007), as well as HP/LT metamorphic paragenesis conditions that are not conducive to complete homogenization and equilibrium conditions. For example, the absence of feldspar could modulate the magnitude of the Eu anomaly, whereas the absence of garnet in these lithologies ($T < 450°C$) during the prograde path would inhibit HREE depletion. Furthermore, magmatic TE signatures in some of the zircon rims indicate a recrystallization/precipitation mechanism for zircon rim formation which favors inheritance of immobile elements from the magmatic core rather than longer length scale diffusive transport or directly precipitating from an externally-derived fluid. The process of rim recrystallization does not require the presence of a fluid source (Tomaschek et al., 2003) to remove or add cations to the zircon lattice (Hoskin, 2005). The interpretation of Eocene rim recrystallization is also supported by $\delta^{18}O$ values that are indistinguishable from their cores. In addition, CL images reveal that Eocene rims preserve the primary textural characteristics of their protolith zircons (Martin et al., 2008; Chen et al., 2010; Fig. 9, S2).

6.3.2 Oligocene metamorphic zircon rims require presence of an externally-derived fluid

In contrast to the Eocene rims, the occurrence of Oligocene metamorphic rims is limited to occurrence in metasedimentary samples collected near the CB-CBU contact. Although these rims exist in both CB and CBU metasedimentary rocks, they appear to be absent in zircon from the CB meta-granitoids (this study; Flansburg et al., 2019; Poulaki et al., 2019). The REE patterns in the Oligocene rims are distinctly different from both their cores and the population of Eocene rims. Major differences include an overall enrichment of MREE, HREE, U and Hf as well as distinctly lower Th/U values (Figs. 3C, 5A, 7A-C).

Thin sections studied from the samples with Oligocene rims contain garnet pseudomorphs replaced by chlorite (Fig. 8A-I). Higher modal abundances and partition coefficients of garnet can dominate the whole-rock HREE budgets and control the HREE patterns in zircon and studies have shown that garnet and zircon might not equilibrate (Lancaster et al., 2009). Since garnets are enriched in HREE and Hf, the observed Oligocene zircon rim HREE enrichment and higher Hf concentrations suggests growth during or after the retrograde breakdown of garnet. We propose that aqueous fluids drove the breakdown mineral phases like HREE-rich garnet, and less significantly, rutile enriched in Zr, triggering the formation of new zircon rims.

A likely mechanism for the formation of these metamorphic rims might be the exposure of pre-existing zircon grains to fluid-driven retrograde breakdown reactions that result in Zr liberation, making Zr available for zircon growth (e.g., Liermann et al., 2002; Tomaschek et al., 2003; Rubatto and Hermann, 2003b). These fluids then act as medium for TE and contribute to the metamorphic zircon rim formation (e.g., Ayers et al., 2002; Liati & Gebauer, 1999; Rubatto et al., 1999; Zheng et al., 2003). Similar LREE concentrations between core-rim pairs and low Th/U values of these rims agree with many experimental studies of zircon formed from aqueous fluids that indicate fluids are capable of transporting only moderate amounts of LREE, Th, and U (Hermann, 2002; Hermann et al., 2006; Hermann and Green, 2001; Kessel et al., 2005; Klimm et al., 2008; Spandler et al., 2008).

Studies of natural samples containing zircon formed from aqueous fluid present extremely low Th/U values (<0.05) (e.g., Rubatto and Hermann, 2003; Zheng et al., 2007a). Additionally, limited experimental data from Ayers & Watson (1991) and Liermann et al. (2002) have suggested that Zr solubility in aqueous fluids is controlled by pressure, temperature, and pH. Hence, when zircon reacts with a fluid phase during HP or HT conditions, the grain will re-equilibrate by enhancing the HFSEs mobility (Tomaschek et al., 2003).

6.4 The origin of metasomatic fluids

The petrology and TE of samples with Oligocene rims indicate the presence of fluids during retrograde metamorphism. Fluids are most likely to be derived by the subducting slab as dehydration reactions cause the release of water from subducting sedimentary and volcanic rocks. Oxygen isotope ratios between 8.6 and 9.0‰ suggest zircon rim formation in the presence of ^{18}O-enriched fluids likely representing slab-derived fluids from dehydrating sediments (Sharp et al., 2007 and references therein) during the Oligocene (Fig. 11B) that were also responsible for the fluid-driven breakdown of garnet. The presence of cauliflower-like textures in the Oligocene zircon rims also indicates the importance of aqueous fluids for their formation. Oxygen isotope ratios, TE, the presence of cauliflower-like textures supports the interpretation that the Oligocene zircon rims are metamorphic in nature and associated with a metasomatic fluid. Furthermore, the proximity of these samples to a major lithologic contact and that a high-permeability zone created by the CBU-CB contact facilitated fluid transport. The permeability of metasedimentary rocks can be larger than that of granitoid rocks (Spear and Rumble, 1986) which could have allowed fluid

circulation proximal to the CB-CBU contact, and may explain why aqueous fluids do not appear to have played a major role in formation of the Eocene-age rims.

6.5 Tectonic implications

The nature and role of the contact between the CBU and the CB has been debated and variably interpreted as either extensional, contractional, or depositional/para-autochthonous. On Ios, it has been interpreted as either an Eocene-Oligocene south-dipping extensional shear zone (the South Cyclades Shear Zone—SCSZ), truncated by the Miocene south-dipping Ios detachment fault (e.g., Baldwin and Lister, 1998; Forster et al., 2020; Forster and Lister, 1999, 2008, 2010; Lister et al., 1984; Mizera and Behrmann, 2015; Forster et al., 2020) or, as an Eocene subduction-related top-to-south thrust fault, the South Cyclades Thrust (SCT) (Huet et al., 2009; van der Maar & Jansen, 1983) that was later reactivated during exhumation as a top-to-north low-angle normal fault (Augier et al., 2014; Huet et al., 2009). Poulaki et al. (2019) interpreted the relationship between the CBU and CB on Sikinos as para-autochthonous, linking the meta-sedimentary units below and above the contact to a semi-intact and coherent stratigraphic succession. More recently, Ring and Glondy (2021) argued for the contact on Sikinos to represent an Oligocene thrust that was reactivated as a north-dipping extensional low-angle normal fault final exhumation. Their interpretation is in part based on a potential pressure jump between the two units, although the most recent peak pressure estimates for the CB and CBU are similar. Huet, (2010) reported PT conditions for the CB of 16.5 ± 1.3 kbar for 500 ± 20°C by pseudosection modeling on Ios revising previous estimates of 11 kbar for 475°C (Gupta and Bickle, 2004). The PT estimates for the CB are similar to those of the CBU of 18.5 ± 1 kbar for 510 ± 20°C (Augier et al., 2015), indicating either no pressure difference or only a weak pressure gradient between the CB and CBU, given the overlapping metamorphic conditions.

In this study, TE, U-Pb and $\delta^{18}O$ analyses of metamorphic zircon rims from meta-sedimentary samples from the CB and CBU provide insights into the metamorphic evolution of the Southern Cyclades from subduction to exhumation and allow us to place further constraints on the nature and role of this contact and better understand the tectonic evolution of this region. The presence of Eocene zircon rims in both the CB and the CBU supports the scenario that these units were either subducted together or juxtaposed during subduction and experienced contemporaneous subduction metamorphism (Figs. 3, 11A). These results supplement the interpretation of the CBU as para-autochthonous with respect to the CB since it supports that the units where subducted

790 together, (Poulaki et al., 2019; Flansburg et al., 2019) based on detailed detrital zircon provenance
791 data that demonstrates that the early CBU (Permo-Triassic) was deposited directly on top of, or in
792 close proximity to, the basement units of the CB. Following long-lived Mesozoic rifted and passive
793 margin deposition, both units entered the subduction channel in the early Cenozoic as evidenced
794 by the shared Cenozoic metamorphic evolution (e.g., Huet et al., 2009). This interpretation is in
795 contrast to a proposed Oligocene juxtaposition of the CB and CBU during back-arc extension and
796 the final stages of exhumation, implying that the CB-CBU contact acted as an extensional shear
797 zone and/or low-angle normal fault during the formation of the Ios metamorphic core complex
798 (Lister et al., 1984; Forster and Lister, 1999; 2008; Baldwin and Lister, 1998; Forster et al., 2020).
799 However, the shared Oligocene metamorphic history of fluid-driven garnet breakdown and zircon
800 rim growth localized along the CB-CBU contact, appears to contradict this later scenario that
801 suggests that the contact is a low angle normal fault. This very localized zone of fluid alteration in
802 both the CB and CBU would not be possible if the contact had been reactivated as a large-
803 displacement extensional fault zone in post-Oligocene times. Hence, the evidence for synchronous
804 HP/LT metamorphism in both the CBU and CB (Fig. 3; Huet et al., 2009) and the spatial
805 correspondence of Oligocene retrograde metamorphism along the contact, in conjunction with
806 published provenance data, support the interpretation that the CBU and CB formed a coherent pre-
807 subduction tectonic unit and argue against major Cenozoic extensional displacement along the CB-
808 CBU interface.

809 Combined zircon U-Pb and TE data document the occurrence of a metamorphic event in
810 the Oligocene that resulted in zircon overgrowth due to static, fluid-driven retrograde breakdown
811 reactions along the CB-CBU contact zone, affecting both units simultaneously. These fluids are
812 likely deriving from the subducted sediments and they result in retrograde re-hydration of the rocks
813 following the exhumation path (Fig. 11B). Given the preservation of the chlorite replacement
814 texture it is unlikely that the Oligocene alteration was accompanied by penetrative ductile
815 deformation, but it is possible that brittle deformation may have facilitated fluid flow along the
816 high permeability zone of the CB-CBU contact. HREE enrichment in Oligocene zircon rims is
817 consistent with petrographically observed garnet breakdown along the CB/CBU contact zone.

818 Previous work on Naxos Island (Fig. 1), located ~30 km north of Sikinos and Ios, also
819 identified a younger generation of zircon rims at ~20 Ma. The authors related these rims to syn-

extensional Miocene magmatism (Bolhar et al., 2017; Martin et al. 2006) on the basis of low LREE concentrations attributed to crystallization in equilibrium with the mafic host rock. However, this is not the case for the Oligocene zircon rims identified in Sikinos and Ios that are characterized by higher HREE concentrations and texturally linked to localized breakdown. More importantly, the nature and origin of the fluid phase triggering this localized retrograde metamorphism is indicated by the zircon rim $\delta^{18}O$ values. These data agree with the temporal occurrence of arc magmatism, which did not invade the central Cyclades until the early-middle Miocene (Andriessen et al., 1979), postdating the formation of most zircon rims in Sikinos and Ios.

A likely scenario for the origin of fluid is the dehydration of younger sediment in the underlying subduction channel and upward migration and infiltration along the more permeable CBU-CB contact zone. Regionally, it has been shown that the Basal Unit was emplaced below the CBU in the subduction zone in the latest Eocene or Oligocene (e.g., Shaked et al., 2000) (Fig. 11B). Prograde dehydration of sediments, such as the latest Eocene Almyropotamos Flysch (e.g., Dubois and Bignot, 1979; Shaked et al., 2000) atop the Basal Unit or other younger subducted sediments in the subduction zone below the CBU, could provide aqueous fluids that infiltrate the previously underplated CB and CBU units in the roof of the subduction zone prior to the sweep of late Cenozoic arc magmatism and exhumation during back-arc extension (Fig. 11B).

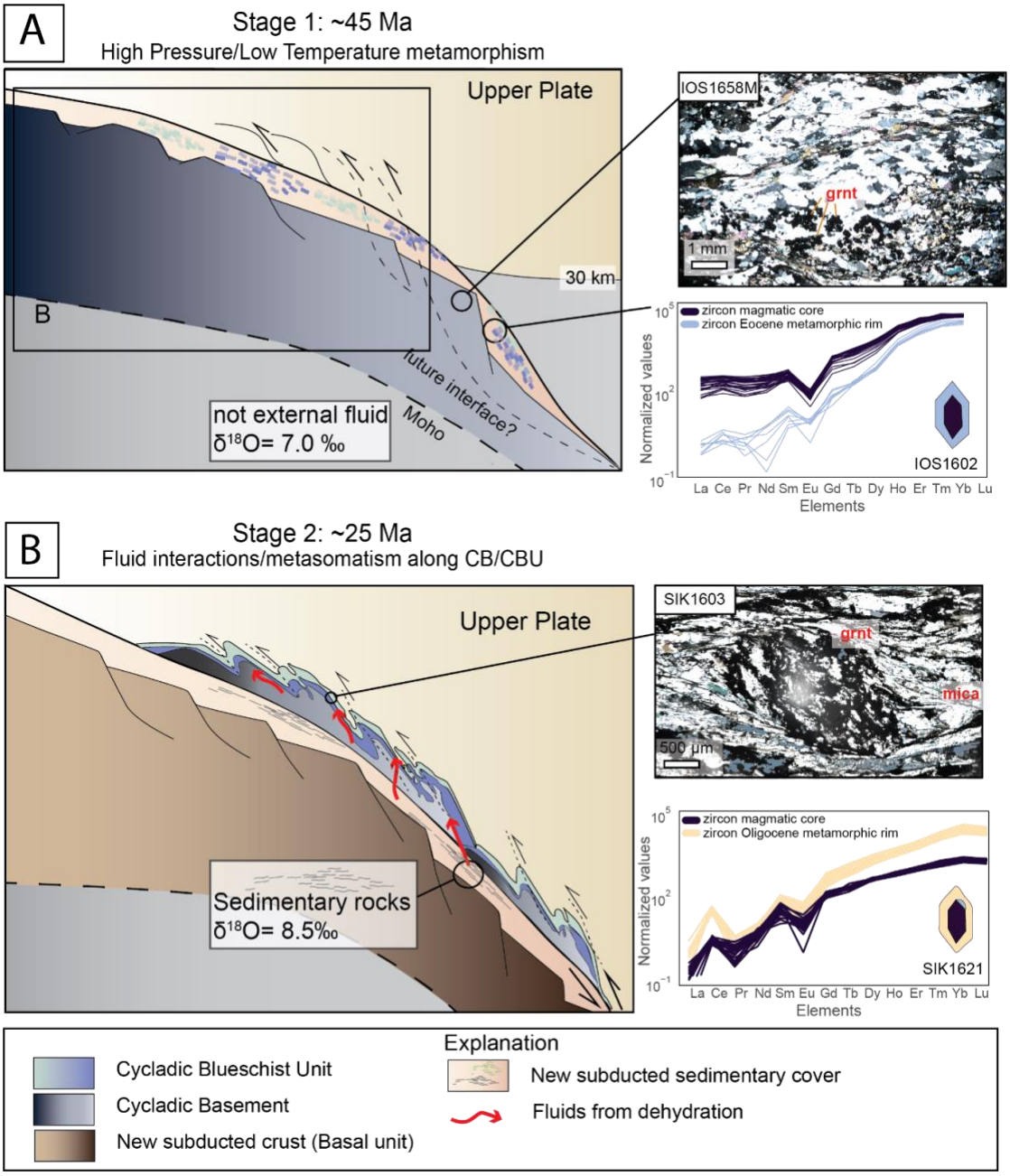

Figure 11: Tectono-metamorphic evolution of CBU and CB from subduction to subsequent exhumation. (A) 55-45 Ma: Subduction of CB and CBU during High-Pressure/Low-Temperature metamorphism. Thin section from granitic sample (IOS1658M) within the CB with preserved garnets. Spider diagram from single grain (sample IOS1621) shows strong depletion in the HREE and LREE of the Eocene metamorphic rim. (B) 30-20 Ma: Partial exhumation of the CB and CBU. Migration of fluids from dehydration of subducted sediments towards the partially exhumed CB and CBU. Red arrows show the circulation of fluids along the CB-CBU contact. Thin section from CBU sample (SIK1603) collected along the CB-CBU contact shows garnet breaking down and being replaced by mica. Spider diagram from a single grain (SIK1603) shows enrichment in the HREE of the Oligocene metamorphic rims.

847 6.6. Implications for Metamorphic Zircon Petrochronology

848 More than a decade of petrochronology research has demonstrated that zircon is part of
849 the metamorphic mineral assemblage and can grow in response to metamorphic reactions, such as
850 garnet, rutile, hornblende breakdown (Degeling et al., 2001; Kohn and Kelly, 2018). Rubatto
851 (2017) summarized how zircon TE compositions in high-grade metamorphic rocks and migmatites
852 can be linked to parameters, such as protolith composition, metamorphic mineral paragenesis,
853 temperature and pressure, and fluid flux. However, less is known about zircon petrochronology in
854 low- to medium-grade metamorphic rocks. This study demonstrates the power of depth-profile
855 split-stream LA-ICP-MS analysis in unraveling the timing and tectono-metamorphic conditions of
856 multiple metamorphic events from thin zircon rims in medium-grade (~500 ºC) HP/LT rocks that
857 are devoid of garnet (Sample IOS1602), or garnet is not present when the zircon rims are forming.
858 Both one-dimensional depth profiling of unpolished zircon grains and grain-internal two-
859 dimensional mapping of polished grains, are critical for understanding temporally distinct zircon
860 growth domains and metamorphic processes taking place during their formation.

861 Results of this study suggest that REE signatures of metamorphic zircon in moderate-grade
862 HP/LT metamorphic rocks in subduction complexes do not adhere to diagnostic REE signatures
863 considered to be well-documented in higher-grade garnet- or melt-bearing metamorphic rocks
864 (e.g., Lancaster et al. 2009; Rubatto, 2017). However, many rocks from the Cycladic complex do
865 not contain classic medium to high-grade metamorphic minerals, such as garnet, and therefore lack
866 mineral phases that strongly dominate REE budgets during zircon growth. REE signatures of
867 HP/LT Eocene zircon rims show a high degree of variability in Ce/Ce* vs Sm/La, spanning the
868 range of compositions from magmatic to hydrothermal, with zircon rims either mimicking the
869 composition of their magmatic core or plotting near the hydrothermal field (Fig. 7 J-L, from
870 Hoskin, 2005). The lack of classic HP/LT metamorphic zircon REE patterns, such as flat H-MREE
871 slopes is likely linked to the origin of the zircon rims that either stem from zircon recrystallization,
872 inheriting the REE signature of their corresponding core, or metamorphic reactions liberating Zr
873 and promoting zircon overgrowths (this study; Tomaschek et al., 2003). Zircon growth and REE
874 composition appear to reflect variable local protolith composition, mineral paragenesis, and P-T
875 conditions. REE homogeneity was limited by restricted diffusion length scales, local phase
876 equilibria, and reaction kinetics, resulting in spatial REE heterogeneity that did not produce a
877 consistent and diagnostic metamorphic REE signature.

878 In contrast to the REE signatures in these Eocene metamorphic zircon rims, the Th/U and
879 Hf concentrations are significantly more uniform and decoupled from the REE variability.
880 Systematically lower zircon Th/U (<0.3) in zircon rims from these rocks is a more consistent and
881 diagnostic indicator for the metamorphic nature. This is likely due to the amplified dependence of
882 Th/U on the occurrence of specific accessory minerals during prograde metamorphism such as
883 allanite or monazite. Another important factor might be the fluid mobility of U under oxidized
884 conditions (Garber et al., 2020). In contrast to REE, U therefore might better reflect the
885 metamorphic nature of these lower-grade zircons in the absence of mineral assemblages that
886 dominate the REE budget. Other studies of similar subduction-related metamorphic rocks have
887 also demonstrated diagnostic low Th/U values for metamorphic zircon rims (e.g., Hoskin &
888 Schaltegger, 2003; Rubatto, 2017; Seymour et al., 2018).

889 The Oligocene zircon rims are linked to garnet breakdown, hence, the REE patterns are
890 more uniform and more consistently plot outside the magmatic field and closer to the hydrothermal
891 domain (Fig. 7 J-L). “Cauliflower” texture and oxygen isotope ratios point out to an externally
892 derived fluid that triggered garnet breakdown, appear to have promoted zircon overgrowth with
893 more homogeneous, enriched HREE signatures that are systematically different from their
894 corresponding zircon cores. Hence, metamorphic Zr availability was likely more important for
895 Oligocene zircon growth than in-situ zircon recrystallization. However, similar to the Eocene
896 cores, zircon Th/U is consistently very low (<0.1) and diagnostic of metamorphic zircon growth
897 in these rocks under these conditions. The ultra-low Th/U appears to be driven by either removal
898 or immobility of Th (<300 ppm) and also dramatic U enrichment (500 to 10,000 ppm) likely related
899 to U fluid mobility (Fig. 7G-I).

900 This study illustrates the complexities of metamorphic geochemical fingerprinting in low-
901 to medium-grade subduction complexes, but it also displays the power of a more comprehensive
902 characterization of zircon via U-Pb dating, TE depth-profiling and two-dimensional mapping
903 analyses coupled with oxygen isotopic determinations used to reconstruct both the prograde and
904 retrograde metamorphic evolution and the role of fluids in subduction zones. This integrative
905 approach is transportable and should help resolve important questions regarding depositional ages,
906 timing and conditions of metamorphism, as well as fluid-rock interactions in low- to medium-
907 grade subduction metamorphic rocks like the Franciscan complex in California or the Sanbagawa

belt in Japan. The methodology approach conducive to the study of the bulk metamorphic rocks should also help counteract the strong traditional bias introduced by the focus on high-grade exotic blocks contained within subduction mélanges.

7. CONCLUSIONS

On Sikinos and Ios islands in the Cyclades, Greece, both the CB and CBU preserve two distinct metamorphic zircon age modes during the Eocene and Oligocene. This distinction was confirmed with a suite of geochronologic, and geochemical analyses of zircon grains collected from both islands. The Eocene rims are likely related to a HP/LT metamorphic event as also shown in previously reported ages in the literature associated with the Hellenic subduction zone. The presence of Eocene rims in both CB and CBU samples indicates a shared metamorphic history, implying that these units were subducted and metamorphosed contemporaneously. The second generation of rims of Oligocene age are recorded only in samples collected along a major lithologic contact between the CB and the CBU. We suggest that the occurrence of these rims was influenced by higher permeability along the contact, where metasomatic fluids were likely derived from sediment dehydration from the subducting slab and localized during greenschist-facies metamorphism indicating that the units exhumed together without significant displacement.

By systematically combining U-Pb, REE, and oxygen isotope measurements we gain information regarding the petrochronology of the medium-grade HP/LT Cycladic subduction complex and show that Eocene rims exhibit a wide spread of REE signatures that do not yield consistent patterns that are diagnostic of metamorphic growth, likely due to zircon inheritance, local protolith control, metamorphic conditions, and limited equilibrium. The similar REE concentrations and $\delta^{18}O$ values of the rims to their corresponding cores suggests that these rims were formed during recrystallization/precipitation in the absence of significant amounts of externally derived fluid. Oligocene zircon rims, in contrast, reveal REE patterns that are far more uniform and consistent with metamorphic signatures. Growth of these rims occurred in the presence of an external fluid phase from dehydration of sediments, as documented by the oxygen isotope ratios, that promoted both a more homogeneous environment and retrograde break-down reactions of Zr-liberating and HREE-dominating phases (garnet). Despite the complex REE variability, metamorphic rims displayed a much more consistent low to ultra-low Th/U that is decoupled from both the core Th/U and the rim REE signatures. Thus, when trying to identify and understand metamorphic zircon growth in moderate-grade metamorphic rocks, Th/U might still be

a powerful indicator, while REE values can be more complex than in high-temperature/anatectic zircon due to effects related to local paragenesis, diffusion length scales, and disequilibrium.

The results of this study demonstrate how the combination of TE, U-Pb ages, $\delta^{18}O$, and age maps can show the age and chemistry of zircon rims. Since there are relatively good constraints on the regional geologic context, we can further establish our understanding of how zircon records the different metamorphic stages of subducted and exhumed rocks in low to medium grade HP/LT rocks. In most cases, metamorphic zircon growth is complicated and a function of Zr availability, protolith, mineral assemblage present while zircon form; controlling factors influencing the precipitation of Zr-saturated fluids may vary.

8. ACKNOWLEDGMENTS

The project was financially supported by two 2017 Geological Society of America Graduate Student Research Grants and two Jackson School of Geosciences Off Campus Research Awards (awarded to Poulaki and Flansburg), the Chevron (Gulf) Endowment (Stockli), UTChron laboratory funds, and NSF Grant (EAR-1725110) awarded to Barnes, Stockli, and Behr. WiscSIMS is supported by NSF (EAR-2004618) and the University of Wisconsin-Madison. JWV and KK are funded by the European Research Council (ERC-2019-SyG-856555). The authors would like to thank Brandon D. Shuck for his help on the development of the Python codes. Additionally, we are thankful to Brandon D. Shuck, Catherine H. Ross and Mark Cloos for the insightful discussion and improving earlier versions of the manuscript. We also thank Priyanka Periwal from Bureau of Economic Geology, UT Austin for collecting the panchromatic CL images and Thomas Etzel and for his help acquiring monochromatic CL images. We would also like to thank Balz Kamber and Dhilip Kumar for the editorial handling of the manuscript and Michael Bröcker and one anonymous reviewer for the constructive feedback that greatly improved the manuscript.

9. REFERENCES

Agard, P., Plunder, A., Angiboust, S., Bonnet, G., & Ruh, J. (2018). The subduction plate interface: rock record and mechanical coupling (from long to short timescales). *Lithos*, *320*, 537-566.

Andriessen, P. A. M., Banga, G., & Hebeda, E. H. (1987). Isotopic age study of pre-Alpine rocks in the basal units on Naxos, Sikinos, and Ios, Greek Cyclades. *Geologie En Mijnbouw*, *66*, 3– 14.

968 Andriessen, P. A. M., Boelrijk, N. A. I. M., Hebeda, E. H., Priem, H. N. A., Verdurnen, E. T., &
969 Verschure, R. H. (1979). Dating the events of metamorphism and granitic magmatism in the
970 Alpine Orogen of Naxos (Cyclades, Greece). *Contributions to Mineralogy and Petrology*, *69*(3),
971 215-225.

972 Andriessen, P. A. M., Hebeda, E. H., Simon, O. J., & Verschure, R. H. (1991). Tourmaline K Ar ages
973 compared to other radiometric dating systems in Alpine anatectic leucosomes and metamorphic
974 rocks (Cyclades and southern Spain). *Chemical Geology*, *91*(1), 33-48.

975 Andriessen, P. A. M., Boelrijk, N. A. I. M., Hebeda, E. H., Priem, H. N. A., Verdurnen, E. A. T., &
976 Verschure, R. H. (1979). Dating the events of metamorphism and granitic magmatism in the
977 Alpine orogen of Naxos (Cyclades, Greece). *Contributions to Mineralogy and Petrology*, *69*(3),
978 215– 225. https://doi.org/10.1007/BF00372323

979 Appleby, S. K., M. R. Gillespie, C. M. Graham, R. W. Hinton, G. J. H. Oliver, N. M. Kelly, and EIMF
980 (2010), Do S-type granites commonly sample infracrustal sources? New results from an
981 integrated O, U-Pb and Hf isotope study of zircon*, Contributions to Mineralogy and Petrology*.,
982 160, 115–132.

983 Augier, R., Jolivet, L., Gadenne, L., Lahfid, A., & Driussi, O. (2015). Exhumation kinematics of the
984 Cycladic Blueschists unit and back-arc extension, insight from the Southern Cyclades (Sikinos
985 and Folegandros Islands, Greece). *Tectonics*, 34, 152– 185.
986 https://doi.org/10.1002/2014TC003664

987 Ayers, J. C., & Watson, E. B. (1991). Solubility of apatite, monazite, zircon, and rutile in supercritical
988 aqueous fluids with implications for subduction zone geochemistry. *Philosophical Transactions*
989 *of the Royal Society of London. Series A: Physical and Engineering Sciences*, *335*(1638), 365-
990 375.

991 Ayers, J. C., Dunkle, S., Gao, S., & Miller, C. F. (2002). Constraints on timing of peak and retrograde
992 metamorphism in the Dabie Shan ultrahigh-pressure metamorphic belt, east-central China, using
993 U–Th–Pb dating of zircon and monazite. *Chemical Geology*, *186*(3-4), 315-331.

994 Baldwin, S. L., & Lister, G. S. (1998). Thermochronology of the South Cyclades Shear Zone, Ios,
995 Greece: Effects of ductile shear in the argon partial retention zone. *Journal of Geophysical*
996 *Research, 103*(B4), 7315– 7336. https://doi.org/10.1029/97JB03106

997 Bea, F. (1996). Residence of REE, Y, Th and U in granites and crustal protoliths; implications for the
998 chemistry of crustal melts. *Journal of Petrology*, *37*(3), 521-552.

999 Bebout, G. E., & Penniston-Dorland, S. C. (2016). Fluid and mass transfer at subduction interfaces—
1000 The field metamorphic record. *Lithos, 240*, 228-258.

1001 Bingen, B., Austrheim, H., & Whitehouse, M. (2001). Ilmenite as a source for zirconium during high-
1002 grade metamorphism? Textural evidence from the Caledonides of western Norway and
1003 implications for zircon geochronology. *Journal of Petrology*, *42*(2), 355-375.

1004 Bolhar, R., Ring, U., & Ireland, T. R. (2017). Zircon in amphibolites from Naxos, Aegean Sea, Greece:
1005 origin, significance and tectonic setting. Journal of Metamorphic *Geology, 35*(4), 413– 434.
1006 https://doi.org/10.1111/jmg.12238

1007 Bröcker, M., Kreuzer, H., Matthews, A., & Okrusch, M. (1993). $^{40}Ar/^{39}Ar$ and oxygen isotope studies
1008 of polymetamorphism from Tinos Island, Cycladic blueschist belt, Greece. *Journal of*
1009 *metamorphic Geology*, *11*(2), 223-240.

1010 Bröcker, M., Bieling, D., Hacker, B., Gans, P., 2004. High-Si phengite records the time of greenschist
1011 facies overprinting: implications for models suggesting megadetachments in the Aegean Sea.
1012 Journal of Metamorphic Geology 22, 427–442.

1013 Bröcker M, Baldwin S, Arkudas R. (2013). The geological significance of 40Ar/39Ar and Rb-Sr white
1014 mica ages from Syros and Sifnos, Greece: A record of continuous (re)crystallization during
1015 exhumation? Journal of Metamorphic Geology, 31, 629–646.

1016 Bröcker, M. and Franz, L., 1998. Rb–Sr isotope studies on Tinos Island (Cyclades, Greece): additional
1017 time constraints for metamorphism, extent of infiltration-controlled overprinting and
1018 deformational activity. *Geological Magazine, 135*(3), pp.369-382.

1019 Brun, J. P., & Faccenna, C. (2008). Exhumation of high-pressure rocks driven by slab rollback. Earth
1020 and Planetary Science Letters, 272(1-2), 1-7.

1021 Burnham, A. D., & Berry, A. J. (2012). An experimental study of trace element partitioning between
1022 zircon and melt as a function of oxygen fugacity. *Geochimica et Cosmochimica Acta*, *95*, 196-
1023 212.

1024 Cao, P., Park, H. S., & Lin, X. (2013). Strain-rate and temperature-driven transition in the shear
1025 transformation zone for two-dimensional amorphous solids. *Physical Review E*, *88*(4), 042404.

1026 Cao, S., Neubauer, F., Bernroider, M., & Liu, J. (2013). The lateral boundary of a metamorphic core
1027 complex: The Moutsounas shear zone on Naxos, Cyclades, Greece. *Journal of structural*
1028 *geology*, *54*, 103-128.

1029 Cavosie AJ, Valley JW, Wilde SA, EIMF (2006) Correlated microanalysis of zircon: Trace element,
1030 $\delta^{18}O$, and U-Th-Pb isotopic constraints on the igneous origin of complex >3900 Ma detrital grains.
1031 Geochim Cosmochim Acta 70: 5601-5616.

1032 Chen, R. X., Zheng, Y. F., & Xie, L. (2010). Metamorphic growth and recrystallization of zircon:
1033 distinction by simultaneous in-situ analyses of trace elements, U–Th–Pb and Lu–Hf isotopes in
1034 zircons from eclogite-facies rocks in the Sulu orogen. *Lithos*, *114*(1-2), 132-154.

1035 Cisneros, M., Barnes, J., Behr, W. M., Kotowski, A. J., Stockli, D., & Soukis, K. (in press). Insights
1036 from elastic thermobarometry into exhumation of high-pressure metamorphic rocks from Syros,
1037 Greece. Solid Earth.

1038 Cliff, R. A., Bond, C. E., Butler, R. W. H., & Dixon, J. E. (2017). Geochronological challenges posed
1039 by continuously developing tectonometamorphic systems: Insights from Rb–Sr mica ages from
1040 the Cycladic Blueschist Belt, Syros (Greece). Journal of Metamorphic Geology, 35(2), 197–211.

1041 Cloos, M. (1993). Lithospheric buoyancy and collisional orogenesis: Subduction of oceanic plateaus,
1042 continental margins, island arcs, spreading ridges, and seamounts. Geological Society of
1043 America Bulletin, 105(6), 715-737.

1044 Coleman, M., Dubosq, R., Schneider, D. A., Grasemann, B., & Soukis, K. (2019). Along-strike
1045 consistency of an extensional detachment system, West Cyclades, Greece. *Terra Nova*, *31*(3),
1046 220-233.

1047 Degeling, H., Eggins, S., & Ellis, D. J. (2001). Zr budgets for metamorphic reactions, and the
1048 formation of zircon from garnet breakdown. *Mineralogical Magazine*, *65*(6), 749-758.

1049 Dragovic, B., Baxter, E. F., & Caddick, M. J. (2015). Pulsed dehydration and garnet growth during
1050 subduction revealed by zoned garnet geochronology and thermodynamic modeling, Sifnos,
1051 Greece. *Earth and Planetary Science Letters*, *413*, 111-122.

Dubois, R., & Bignot, G. (1979). Nummulitic Hard-Ground At The Top Of The Almyropotamos Cretaceous Series (Euboa, Greece)-Its Geological Implications. *Comptes Rendus Hebdomadaires Des Seances De L Academie Des Sciences Serie D*, *289*(14), 993.

Elliott, T., Plank, T., Zindler, A., White, W., & Bourdon, B. (1997). Element transport from slab to volcanic front at the Mariana arc. *Journal of Geophysical Research: Solid Earth*, *102*(B7), 14991-15019.

Flansburg, M. E., Stockli, D. F., Poulaki, E. M., & Soukis, K. (2019). Tectono-magmatic and stratigraphic evolution of the Cycladic basement, Ios Island, Greece. *Tectonics*, *38*(7), 2291-2316.

Forster, M., Koudashev, O., Nie, R., Yeung, S., & Lister, G. (2020). $^{40}Ar/^{39}Ar$ thermochronology in the Ios basement terrane resolves the tectonic significance of the South Cyclades Shear Zone. *Geological Society, London, Special Publications*, *487*(1), 291-313.

Forster, M., & Lister, G. (2008). Dating movement in shear zones: The example of the South Cyclades Shear Zone, Ios, Aegean Sea, Greece. IOP Conference Series: *Earth and Environmental Science, 2*, 012004. https://doi.org/10.1088/1755-1307/2/1/012004

Forster, M. A., & Lister, G. S. (1999). Exhumation processes: Normal faulting, ductile flow and erosion. In U. Ring, M. T. Brandon, G. S. Lister, & S. D. Willet (Eds.), *Geological Society, London, Special Publications, 154*, 305– 323. https://doi.org/10.1144/GSL.SP.1999.154.01.14

Forster, M. A., & Lister, G. S. (2010). Argon enters the retentive zone: Reassessment of diffusion parameters for K-feldspar in the South Cyclades Shear Zone, Ios, Greece. In M. I. Spalla, A. M. Marotta, & G. Gosso (Eds.), Advances in interpretation of geological processes: Refinement of multi-scale data and integration in numerical modeling, *Geological Society, London, Special Publications, 332,* 17– 34. https://doi.org/10.1144/SP332.2

Fraser, G., Ellis, D., & Eggins, S. (1997). Zirconium abundance in granulite-facies minerals, with implications for zircon geochronology in high-grade rocks. *Geology, 25*(7), 607-610. https://doi.org/10.1130/0091-7613(1997)025<0607:ZAIGFM>2.3.CO;2

Fu, B., Paul, B., Cliff, J., Bröcker, M., & Bulle, F. (2012). O-Hf isotope constraints on the origin of zircon in high-pressure melange blocks and associated matrix rocks from Tinos and Syros, Greece. *European Journal of Mineralogy*, *24*(2), 277-287.

Fu, B., Bröcker, M., Ireland, T., Holden, P., & Kinsley, L. P. (2015). Zircon U–Pb, O, and Hf isotopic constraints on Mesozoic magmatism in the Cyclades, Aegean Sea, Greece. *International Journal of Earth Sciences*, *104*(1), 75-87.

Fu, B., Valley, J. W., Kita, N. T., Spicuzza, M. J., Paton, C., Tsujimori, T., ... & Harlow, G. E. (2010). Multiple origins of zircons in jadeitite. *Contributions to Mineralogy and Petrology*, *159*(6), 769-780.

Garber, J. M., Smye, A. J., Feineman, M. D., Kylander-Clark, A. R., & Matthews, S. (2020). Decoupling of zircon U–Pb and trace-element systematics driven by U diffusion in eclogite-facies zircon (Monviso meta-ophiolite, W. Alps). *Contributions to Mineralogy and Petrology*, *175*, 1-25.

Geisler, T., Schaltegger, U., & Tomaschek, F. (2007). Re-equilibration of zircon in aqueous fluids and melts. *Elements*, *3*(1), 43-50.

Grasemann, B., Schneider, D. A., Stockli, D. F., & Iglseder, C. (2012). Miocene bivergent crustal extension in the Aegean: Evidence from the western Cyclades (Greece). *Lithosphere, 4*(1), 23–39. https://doi.org/10.1130/L164.1

Grimes, C. B., John, B. E., Kelemen, P. B., Mazdab, F. K., Wooden, J. L., Cheadle, M. J., ... & Schwartz, J. J. (2007). Trace element chemistry of zircons from oceanic crust: A method for distinguishing detrital zircon provenance. *Geology*, *35*(7), 643-646.

Grimes CB, Ushikubo T, John BE, Valley JW (2011) Uniformly mantle-like $\delta^{18}O$ in zircons from oceanic plagiogranites and gabbros, *Contributions to Mineralogy and Petrology 161*, 13-33

Grimes, C. B., Wooden, J. L., Cheadle, M. J., & John, B. E. (2015). "Fingerprinting" tectono-magmatic provenance using trace elements in igneous zircon. *Contributions to Mineralogy and Petrology*, *170*(5-6), 46.

Gupta, S., & Bickle, M. J. (2004). Ductile shearing, hydrous fluid channeling and high-pressure metamorphism along the basement-cover contact on Sikinos, Cyclades, Greece. *Geological Society, London, Special Publications, 224*(1), 161– 175. https://doi.org/10.1144/GSL.SP.2004.224.01.11

Hacker, B. R. (2008). H_2O subduction beyond arcs. *Geochemistry, Geophysics, Geosystems*, *9*(3), Q03001.

Harley, S. L., & Kelly, N. M. (2007). The impact of zircon–garnet REE distribution data on the interpretation of zircon U–Pb ages in complex high-grade terrains: an example from the Rauer Islands, East Antarctica. *Chemical Geology*, *241*(1-2), 62-87.

Henjes-Kunst, F., & Kreuzer, H. (1982). Isotopic dating of pre-Alpidic rocks from the island of Ios (Cyclades, Greece). Contributions to *Mineralogy and Petrology, 80*(3), 245– 253. https://doi.org/10.1007/BF00371354

Hermann, J. (2002). Allanite: thorium and light rare earth element carrier in subducted crust. *Chemical geology*, *192*(3-4), 289-306.

Hermann, J., & Rubatto, D. (2003). Relating zircon and monazite domains to garnet growth zones: age and duration of granulite facies metamorphism in the Val Malenco lower crust. *Journal of Metamorphic Geology*, *21*(9), 833-852.

Hermann, J., & Green, D. H. (2001). Experimental constraints on high pressure melting in subducted crust. *Earth and Planetary Science Letters*, *188*(1-2), 149-168.

Hermann, J., Spandler, C., Hack, A., & Korsakov, A. V. (2006). Aqueous fluids and hydrous melts in high-pressure and ultra-high pressure rocks: implications for element transfer in subduction zones. *Lithos*, *92*(3-4), 399-417.

Hoskin, P. W. (2005). Trace-element composition of hydrothermal zircon and the alteration of Hadean zircon from the Jack Hills, Australia. *Geochimica et Cosmochimica Acta*, *69*(3), 637-648.

Hoskin, P. W. O., & Black, L. P. (2000). Metamorphic zircon formation by solid-state recrystallization of protolith igneous zircon. *Journal of metamorphic Geology*, *18*(4), 423-439.

Hoskin, P. W., & Schaltegger, U. (2003). The composition of zircon and igneous and metamorphic petrogenesis. *Reviews in mineralogy and geochemistry*, *53*(1), 27-62.

Hoskin, P. W., & Ireland, T. R. (2000). Rare earth element chemistry of zircon and its use as a provenance indicator. *Geology*, *28*(7), 627-630.

Huet, B., Labrousse, L., & Jolivet, L. (2009). Thrust or detachment? Exhumation processes in the Aegean: Insight from a field study on Ios (Cyclades, Greece). *Tectonics, 28,* TC3007. https://doi.org/10.1029/2008TC002397

Huet, B. (2010). *Rhéologie de la lithosphère continentale: L'exemple de la Mer Egée* (Doctoral dissertation, Université Pierre et Marie Curie-Paris VI).

Jackson, S. E., Pearson, N. J., Griffin, W. L., & Belousova, E. A. (2004). The application of laser ablation-inductively coupled plasma-mass spectrometry to in situ U–Pb zircon geochronology. *Chemical geology*, *211*(1-2), 47-69.

Jolivet, L., & Brun, J. P. (2010). Cenozoic geodynamic evolution of the Aegean. *International Journal of Earth Sciences, 99*(1), 109– 138. https://doi.org/10.1007/s00531-008-0366-4

Jolivet, L., Lecomte, E., Huet, B., Denèle, Y., Lacombe, O., Labrousse, L., ... & Mehl, C. (2010). The north cycladic detachment system. *Earth and Planetary Science Letters*, *289*(1-2), 87-104.

Keay, S., & Lister, G. (2002). African provenance for the metasediments and metaigneous rocks of the Cyclades, Aegean Sea, Greece. *Geology, 30*(3), 235– 238. https://doi.org/10.1130/0091-7613(2002)030<0235:APFTMA>2.0.CO;2

Kelly, N. M., & Harley, S. L. (2005). An integrated microtextural and chemical approach to zircon geochronology: refining the Archaean history of the Napier Complex, east Antarctica. *Contributions to Mineralogy and Petrology, 149*(1), 57-84. https://doi.org/10.1007/s00410-004-0635-6

Kelly, N. M., Hinton, R. W., Harley, S. L., & Appleby, S. K. (2008). New SIMS U–Pb zircon ages from the Langavat Belt, South Harris, NW Scotland: implications for the Lewisian terrane model. *Journal of the Geological Society*, *165*(5), 967-981.

Kennedy, A. K., Wotzlaw, J. F., Schaltegger, U., Crowley, J. L., & Schmitz, M. (2014). Eocene zircon reference material for microanalysis of U-Th-Pb isotopes and trace elements. *The Canadian Mineralogist*, *52*(3), 409-421.

Kessel, R., Schmidt, M. W., Ulmer, P., & Pettke, T. (2005). Trace element signature of subduction-zone fluids, melts and supercritical liquids at 120–180 km depth. *Nature*, *437*(7059), 724-727.

1161 Kinny, P. D., & Maas, R. (2003). Lu–Hf and Sm–Nd isotope systems in zircon. *Reviews in mineralogy*
1162 *and geochemistry*, *53*(1), 327-341.

1163 Kita, N.T., Ushikubo, T., Fu, B., Valley, J.W., 2009. High precision SIMS oxygen isotope analysis
1164 and the effect of sample topography. *Chemical geology, 264*, 43–57.

1165 Klimm, K., Blundy, J. D., & Green, T. H. (2008). Trace element partitioning and accessory phase
1166 saturation during H_2O-saturated melting of basalt with implications for subduction zone
1167 chemical fluxes. *Journal of Petrology*, *49*(3), 523-553.

1168 Kohn, M. J. (2016). Metamorphic chronology—a tool for all ages: Past achievements and future
1169 prospects. *American Mineralogist*, *101*(1), 25-42.

1170 Kohn, M. J., & Kelly, N. M. (2018). Petrology and geochronology of metamorphic zircon.
1171 Microstructural geochronology: planetary records down to atom scale, *Wiley, Oxford,* 35-61.
1172 https://doi.org/10.1002/9781119227250.ch2

1173 Korhonen, F. J., Clark, C., Brown, M., Bhattacharya, S., & Taylor, R. (2013). How long-lived is
1174 ultrahigh temperature (UHT) metamorphism? Constraints from zircon and monazite
1175 geochronology in the Eastern Ghats orogenic belt, India. *Precambrian Research*, *234*, 322-350.

1176 Kotowski, A. J., Behr, W. M., Cisneros, M., Stockli, D. F., Soukis, K., Barnes, J. D., & Ortega-Arroyo,
1177 D. (2021). Subduction, underplating, and return flow recorded in the Cycladic Blueschist Unit
1178 exposed on Syros, Greece.

1179 Kylander-Clark, A. R. (2017). Petrochronology by laser-ablation inductively coupled plasma mass
1180 spectrometry. *Reviews in Mineralogy and Geochemistry*, *83*(1), 183-198.

1181 Lagos, M., Scherer, E. E., Tomaschek, F., Münker, C., Keiter, M., Berndt, J., & Ballhaus, C. (2007).
1182 High precision Lu–Hf geochronology of Eocene eclogite-facies rocks from Syros, Cyclades,
1183 Greece. *Chemical Geology*, *243*(1-2), 16-35.

1184 Lancaster P.J., Fu B., Page F.Z., Kita N.T., Bickford M.E., Hill B.M., McLelland J.M., Valley J.W.
1185 (2009) Genesis of metapelitic migmatites in the Adirondack Mts., New York, *Journal of*
1186 *metamorphic petrology, 27,* 41-54

1187 Liati, A., & Gebauer, D. (1999). Constraining the prograde and retrograde PTt path of Eocene HP
1188 rocks by SHRIMP dating of different zircon domains: inferred rates of heating, burial, cooling

and exhumation for central Rhodope, northern Greece. *Contributions to Mineralogy and Petrology, 135*(4), 340-354. https://doi.org/10.1007/s004100050516

Liermann, H. P., Isachsen, C., Altenberger, U., & Oberhänsli, R. (2002). Behavior of zircon during high-pressure, low-temperature metamorphism: case study from the Internal Unit of the Sesia Zone (Western Italian Alps). *European Journal of Mineralogy*, *14*(1), 61-71.

Lister, G. S., & Forster, M. A. (2016). White mica $^{40}Ar/^{39}Ar$ age spectra and the timing of multiple episodes of high-P metamorphic mineral growth in the Cycladic eclogite–blueschist belt, Syros, Aegean Sea, Greece. *Journal of Metamorphic Geology*, *34*(5), 401-421.

Lister, G. S., Banga, G., & Feenstra, A. (1984). Metamorphic core complexes of Cordilleran type in the Cyclades, Aegean Sea, Greece. *Geology, 12*(4), 221– 225. https://doi.org/10.1130/0091-7613(1984)12<221:MCCOCT>2.0.CO;2

Loader, M. A., Wilkinson, J. J., & Armstrong, R. N. (2017). The effect of titanite crystallisation on Eu and Ce anomalies in zircon and its implications for the assessment of porphyry Cu deposit fertility. *Earth and Planetary Science Letters*, *472*, 107-119.

Martin, L. A., Duchêne, S., Deloule, E., & Vanderhaeghe, O. (2008). Mobility of trace elements and oxygen in zircon during metamorphism: consequences for geochemical tracing. *Earth and Planetary Science Letters*, *267*(1-2), 161-174.

Marsh, J. H., & Stockli, D. F. (2015). Zircon U-Pb and trace element zoning characteristics in an anatectic granulite domain: Insights from LASS-ICP-MS depth profiling. *Lithos, 239*, 170– 185. https://doi.org/10.1016/j.lithos.2015.10.017

Martin L., S. Duchêne, E. Deloule, O. Vanderhaeghe (2006). The isotopic composition of zircon and garnet: a record of the metamorphic history of Naxos, Greece *Lithos, 87*, 174-192

McCulloch, M. T., & Gamble, J. A. (1991). Geochemical and geodynamical constraints on subduction zone magmatism. *Earth and Planetary Science Letters*, *102*(3-4), 358-374.

Miller, D. P., Marschall, H. R., & Schumacher, J. C. (2009). Metasomatic formation and petrology of blueschist-facies hybrid rocks from Syros (Greece): Implications for reactions at the slab–mantle interface. *Lithos, 107*(1-2), 53-67.

1216 Mizera, M., & Behrmann, J. H. (2016). Strain and flow in the metamorphic core complex of Ios Island
1217 (Cyclades, Greece). *International Journal of Earth Sciences, 105*(7), 2097– 2110.
1218 https://doi.org/10.1007/s00531-015-1259-y

1219 Möller, A., O'Brien, P. J., Kennedy, A., & Kröner, A. (2002). Polyphase zircon in ultrahigh-
1220 temperature granulites (Rogaland, SW Norway): constraints for Pb diffusion in zircon. *Journal*
1221 *of metamorphic Geology*, *20*(8), 727-740.

1222 Möller, A., O'Brien, P. J., Kennedy, A., & Kröner, A. (2003). Linking growth episodes of zircon and
1223 metamorphic textures to zircon chemistry: an example from the ultrahigh-temperature granulites
1224 of Rogaland (SW Norway). *Geological Society, London, Special Publications*, *220*(1), 65-81.

1225 Moser DE, Bowman JR, Wooden J, Valley JW, Mazdab F, Kita N (2008) Creation of a Continent
1226 recorded in zircon zoning. *Geology 36,* 239-242.

1227 Murali, A. V., Parthasarathy, R., Mahadevan, T. M., & Das, M. S. (1983). Trace element
1228 characteristics, REE patterns and partition coefficients of zircons from different geological
1229 environments—a case study on Indian zircons. *Geochimica et Cosmochimica Acta*, *47*(11),
1230 2047-2052.

1231 Nasdala, L., Lengauer, C. L., Hanchar, J. M., Kronz, A., Wirth, R., Blanc, P., ... & Seydoux-
1232 Guillaume, A. M. (2002). Annealing radiation damage and the recovery of
1233 cathodoluminescence. *Chemical Geology*, *191*(1-3), 121-140.

1234 Odlum, M. L., & Stockli, D. F. (2019). Thermotectonic evolution of the North Pyrenean Agly Massif
1235 during Early Cretaceous hyperextension using multi-mineral U-Pb thermochronometry.
1236 *Tectonics, 38*(5), 1509-1531. **https://doi.org/10.1029/2018TC005298**

1237 Page FZ, Essene EJ, Mukasa SB, Valley JW (2014) A garnet-zircon oxygen isotope record of
1238 subduction and exhumation fluids from the Franciscan Complex, California. *Journal of*
1239 *Petrology, 55,* 103-131. doi:10.1093/petrology/egt062

1240 Page FZ, Cameron EM, Flood CM, Dobbins JW, Spicuzza MJ, Kitajima K, Strickland A, Ushikubo
1241 T, Mattinson CG, and Valley JW (2019) Extreme oxygen isotope zoning in garnet and zircon
1242 from a metachert block in mélange reveals metasomatism at the peak of subduction
1243 metamorphism. *Geology, 47*: 655-658. doi.org/10.1130/G46135.1

1244 Papanikolaou, D.J., 1979. Unités tectoniques et phases de déformations dans l'ile de Samos, Mer
1245 Egée, Grèce. Bull.Soc. Géol. Fr. (7) 21: 745-762.

1246 Papanikolaou, D. (2013). Tectonostratigraphic models of the alpine terranes and subduction history
1247 of the Hellenides. *Tectonophysics*, 595-596, 1– 24. https://doi.org/10.1016/j.tecto.2012.08.008

1248 Paton, C., Hellstrom, J., Paul, B., Woodhead, J. and Hergt, J. 2011. "Iolite: Freeware for the
1249 visualisation and processing of mass spectrometric data*." Journal of Analytical Atomic*
1250 *Spectrometry*. doi:10.1039/c1ja10172b.

1251 Pe-Piper, G., & Piper, D. J. (2007). Neogene backarc volcanism of the Aegean: new insights into the
1252 relationship between magmatism and tectonics. *Special Papers-Geological Society of America*,
1253 *418*, 17.

1254 Perraki, M., & Mposkos, E. (2001). New constraints for the Alpine HP metamorphism of the Ios
1255 basement, Cyclades, Greece. *Bulletin of the Geological Society of Greece, 25*(3), 977– 984.

1256 Petrus, J. A., & Kamber, B. S. (2012). VizualAge: A novel approach to laser ablation ICP-MS U-Pb
1257 geochronology data reduction. *Geostandards and Geoanalytical Research, 36*(3), 247-270.

1258 Poller, U., Huth, J., Hoppe, P., & Williams, I. S. (2001). REE, U, Th, and Hf distribution in zircon
1259 from western Carpathian Variscan granitoids: a combined cathodoluminescence and ion
1260 microprobe study. *American Journal of Science*, *301*(10), 858-867.

1261 Poulaki, E. M., Stockli, D. F., Flansburg, M. E., & Soukis, K. (2019). Zircon U-Pb Chronostratigraphy
1262 and Provenance of the Cycladic Blueschist Unit and the Nature of the Contact with the Cycladic
1263 Basement on Sikinos and Ios Islands, Greece. *Tectonics, 38*(10), 3586-3613.

1264 Pidgeon, R. T. (1992). Recrystallisation of oscillatory zoned zircon: some geochronological and
1265 petrological implications. *Contributions to Mineralogy and Petrology*, *110*(4), 463-472.

1266 Putnis, A. (2002). Mineral replacement reactions: from macroscopic observations to microscopic
1267 mechanisms. *Mineralogical Magazine*, *66*(5), 689-708.

1268 Ring, U., Laws, S. and Bernet, M. 1999. Structural analysis of a complex nappe sequence and late-
1269 orogenic basins from the Aegean Island of Samos, Greece. Journal of Structural Geology, 21,
1270 1575–1601

Ring, U., Layer, P.W., and Reischmann, T., 2001, Miocene high-pressure metamorphism in the Cyclades and Crete, Aegean Sea, Greece: Evidence for large-magnitude displacement on the Cretan detachment: Geology, v. 29, p. 395–398.

Ring, U., Glodny, J., Will, T., & Thomson, S. (2010). The Hellenic subduction system: high-pressure metamorphism, exhumation, normal faulting, and large-scale extension. *Annual Review of Earth and Planetary Sciences*, *38*, 45-76.

Ring, U., & Glodny, J. (2021). The importance of tangential motion in the Central Alps: Kinematic analysis and RbSr dating of mylonitic rocks from the Pennine nappes in the eastern Central Alps. Earth-Science Reviews, 103644.

Royden, L. H. (1993). Evolution of retreating subduction boundaries formed during continental collision. *Tectonics, 12*(3), 629– 638. https://doi.org/10.1029/92TC02641

Rubatto, D. (2002). Zircon trace element geochemistry: partitioning with garnet and the link between U–Pb ages and metamorphism. *Chemical Geology, 184*(1-2), 123-138. https://doi.org/10.1016/S0009-2541(01)00355-2

Rubatto, D. (2017). Zircon: the metamorphic mineral. *Reviews in Mineralogy and Geochemistry*, *83*(1), 261-295.

Rubatto, D., & Angiboust, S. (2015). Oxygen isotope record of oceanic and high-pressure metasomatism: a P–T–time–fluid path for the Monviso eclogites (Italy). *Contributions to Mineralogy and Petrology*, *170*(5-6), 44.

Rubatto, D., & Gebauer, D. (2000). Use of cathodoluminescence for U-Pb zircon dating by ion microprobe: some examples from the Western Alps. In *Cathodoluminescence in geosciences* (pp. 373-400). Springer, Berlin, Heidelberg.

Rubatto, D., & Hermann, J. (2007). Zircon behaviour in deeply subducted rocks. *Elements*, *3*(1), 31-35.

Rubatto, D., Gebauer, D., & Compagnoni, R. (1999). Dating of eclogite-facies zircons: the age of Alpine metamorphism in the Sesia–Lanzo Zone (Western Alps). *Earth and Planetary Science Letters, 167*(3-4), 141-158. https://doi.org/10.1016/S0012-821X(99)00031-X

Rubatto, D., & Hermann, J. (2003). Zircon formation during fluid circulation in eclogites (Monviso, Western Alps): implications for Zr and Hf budget in subduction zones. *Geochimica et Cosmochimica Acta*, *67*(12), 2173-2187.

Rudnick, R. L., Barth, M., Horn, I., & McDonough, W. F. (2000). Rutile-bearing refractory eclogites: missing link between continents and depleted mantle. *Science*, *287*(5451), 278-281.

Schaltegger, U., Fanning, C. M., Günther, D., Maurin, J. C., Schulmann, K., & Gebauer, D. (1999). Growth, annealing and recrystallization of zircon and preservation of monazite in high-grade metamorphism: conventional and in-situ U-Pb isotope, cathodoluminescence and microchemical evidence. *Contributions to Mineralogy and Petrology*, *134*(2-3), 186-201.

Schmidt, M. W., & Poli, S. (1998). Experimentally based water budgets for dehydrating slabs and consequences for arc magma generation. *Earth and Planetary Science Letters*, *163*(1-4), 361-379.

Schmitt, A. K., & Vazquez, J. A. (2017). Secondary ionization mass spectrometry analysis in petrochronology. *Reviews in Mineralogy and Geochemistry*, *83*(1), 199-230.

Schneider, D. A., Grasemann, B., Lion, A., Soukis, K., & Draganits, E. (2018). Geodynamic significance of the Santorini Detachment System (Cyclades, Greece). *Terra Nova, 30*(6), 414–422. https://doi.org/10.1111/ter.12357

Schneider, D. A., Grasemann, B., Lion, A., Soukis, K., & Draganits, E. (2018). Geodynamic significance of the Santorini detachment system (Cyclades, Greece). *Terra Nova*, *30*(6), 414-422.

Schneider, D. A., Senkowski, C., Vogel, H., Grasemann, B., Iglseder, C., & Schmitt, A. K. (2011). Eocene tectonometamorphism on Serifos (western Cyclades) deduced from zircon depth-profiling geochronology and mica thermochronology. *Lithos*, *125*(1-2), 151-172.

Seman, S., Stockli, D. F., & Soukis, K. (2017). The provenance and internal structure of the Cycladic Blueschist Unit revealed by detrital zircon geochronology, Western Cyclades, Greece. Tectonics, 36(7), 1407-1429.

Seymour, N. M., Stockli, D. F., Beltrando, M., & Smye, A. J. (2016). Tracing the thermal evolution of the Corsican lower crust during Tethyan rifting. *Tectonics, 35*(10), 2439-2466. https://doi.org/10.1002/2016TC004178

Seymour, N. M., Strickland, E. D., Singleton, J. S., Stockli, D. F., & Wong, M. S. (2018). Laramide subduction and metamorphism of the Orocopia Schist, northern Plomosa Mountains, west-central Arizona: Insights from zircon U-Pb geochronology. *Geology*, *46*(10), 847-850.

Shaked, Y., Avigad, D., & Garfunkel, Z. (2000). Alpine high-pressure metamorphism at the Almyropotamos window (southern Evia, Greece). *Geological Magazine*, *137*(4), 367-380.

Sharman, G. R., Sharman, J. P., & Sylvester, Z. (2018). detritalPy: A Python-based toolset for visualizing and analysing detrital geo-thermochronologic data. *The Depositional Record, 4*(2), 202-215.

Sharp Z. D. (2007) Principles of stable isotope geochemistry. Pearson Prentice Hall, Upper Saddle River, 1–344

Sláma, J., Košler, J., Condon, D. J., Crowley, J. L., Gerdes, A., Hanchar, J. M., ... & Schaltegger, U. (2008). Plešovice zircon—a new natural reference material for U–Pb and Hf isotopic microanalysis. *Chemical Geology*, *249*(1-2), 1-35.

Soukis, K., & Stockli, D. F. (2013). Structural and thermochronometric evidence for multi-stage exhumation of southern Syros, Cycladic islands, Greece. *Tectonophysics, 595-596,* 148– 164. https://doi.org/10.1016/j.tecto.2012.05.017

Spandler, C., Yaxley, G., Green, D. H., & Rosenthal, A. (2008). Phase relations and melting of anhydrous K-bearing eclogite from 1200 to 1600 C and 3 to 5 GPa. *Journal of Petrology*, *49*(4), 771-795.

Spear, F. S., & Rumble III, D. (1986). Pressure, temperature, and structural evolution of the Orfordville Belt, west-central New Hampshire. *Journal of Petrology*, *27*(5), 1071-1093.

Stockli, D. F., & Stockli, L. (2013). Unlocking provenance secrets from single detrital zircons by U-Pb and trace-element depth-profile laser-ablation-split-stream analysis and (U-Th)/He double dating. *Geological Society of America Abstracts with Programs, 45*(7), 744.

Thomson, S. N., Ring, U., Brichau, S., Glodny, J., & Will, T. M. (2009). Timing and nature of formation of the Ios metamorphic core complex, southern Cyclades, Greece. *Geological Society, London, Special Publications, 321*(1), 139– 167. https://doi.org/10.1144/SP321.7

Tomaschek, F., Kennedy, A. K., Villa, I. M., Lagos, M., & Ballhaus, C. (2003). Zircons from Syros, Cyclades, Greece—Recrystallization and mobilization of zircon during high-pressure metamorphism. *Journal of Petrology, 44*(11), 1977– 2002. https://doi.org/10.1093/petrology/egg067

Trail, D., Watson, E. B., & Tailby, N. D. (2012). Ce and Eu anomalies in zircon as proxies for the oxidation state of magmas. *Geochimica et Cosmochimica Acta*, *97*, 70-87.

Valley, J. W. (2003). Oxygen isotopes in zircon. *Reviews in Mineralogy and Geochemistry*, *53*, 343-385.

Valley, J.W., Kita, N.T., 2009. In situ Oxygen Isotope Geochemistry by Ion Microprobe. In: Fayek, M. (Ed.), *MAC Short Course: Secondary Ion Mass Spectrometry in the Earth Sciences. 41*, 19–63.

Van der Maar, P. A., & Jansen, J. B. H. (1983). The geology of the polymetamorphic complex of Ios, Cyclades, Greece and its significance for the Cycladic Massif. *International Journal of Earth Sciences, 72*(1), 283– 299. https://doi.org/10.1007/BF01765910

P. Vannucchi, F. Remitti, G. Bettelli Geological record of fluid flow and seismogenesis along an erosive subducting plate boundary Nature, 451 (2008), pp. 699-703

Vavra, G., Gebauer, D., Schmid, R., & Compston, W. (1996). Multiple zircon growth and recrystallization during polyphase Late Carboniferous to Triassic metamorphism in granulites of the Ivrea Zone (Southern Alps): an ion microprobe (SHRIMP) study. *Contributions to Mineralogy and Petrology*, *122*(4), 337-358.

Vavra, G., Schmid, R., & Gebauer, D. (1999). Internal morphology, habit and U-Th-Pb microanalysis of amphibolite-to-granulite facies zircons: geochronology of the Ivrea Zone (Southern Alps). *Contributions to Mineralogy and Petrology*, *134*(4), 380-404.

Vermeesch, P. (2012). On the visualisation of detrital age distributions. *Chemical Geology*, *312*, 190-194.

Vho, A., Lanari, P., Rubatto, D., & Hermann, J. (2020). Tracing fluid transfers in subduction zones: an integrated thermodynamic and δ 18 O fractionation modelling approach. *Solid Earth*, *11*(2), 307-328.

Wang X-L, Coble MA, Valley JW, Shu X-J, Kitajima K, Spicuzza MJ, Sun T (2014) Influence of radiation damage on late Jurassic zircon from southern China: Evidence from in situ measurement of oxygen isotopes, laser Raman, U-Pb ages, and trace elements. *Chemical Geology*., 389: 122-136.

Wang, Y., Zhang, A., Fan, W., Zhao, G., Zhang, G., Zhang, Y., ... & Li, S. (2011). Kwangsian crustal anatexis within the eastern South China Block: geochemical, zircon U–Pb geochronological and Hf isotopic fingerprints from the gneissoid granites of Wugong and Wuyi–Yunkai Domains. *Lithos*, *127*(1-2), 239-260.

Whitehouse, M. J., & Platt, J. P. (2003). Dating high-grade metamorphism—constraints from rare-earth elements in zircon and garnet. *Contributions to Mineralogy and Petrology*, *145*(1), 61-74.

Wijbrans, J. R., & McDougall, I. (1988). Metamorphic evolution of the Attic Cycladic Metamorphic Belt on Naxos (Cyclades, Greece) utilizing $^{40}Ar/^{39}Ar$ age spectrum measurements. *Journal of Metamorphic Geology*, *6*(5), 571-594.

Williams, I. S. (2001), Response of detrital zircon and monazite, and their U-Pb isotopic systems, to regional metamorphism and host-rock partial melting, Cooma Complex, southeastern Australia, *Australian Journal of Earth Sciences., 48*(4), 557–580.

Williams, I. S., Buick I. S., and Cartwright I. (1996), An extended episode of early Mesoproterozoic fluid flow in the Reynolds Range, central Australia, *Journal of Metamorphic Geology*, *14*, 29–47.

Woodhead, J., Hellstrom, J., Hergt, J., Greig, A. & Maas, R (2007) Isotopic and elemental imaging of geological materials by laser ablation Inductively Coupled Plasma mass spectrometry. *Journal of Geostandards and Geoanalytical Research, 31*, 331-343.

Yakymchuk, C., Kirkland, C. L., & Clark, C. (2018). Th/U ratios in metamorphic zircon. *Journal of Metamorphic Geology*, *36*(6), 715-737.

Yuan, H. L., Gao, S., Dai, M. N., Zong, C. L., Günther, D., Fontaine, G. H., ... & Diwu, C. (2008). Simultaneous determinations of U–Pb age, Hf isotopes and trace element compositions of zircon

by excimer laser-ablation quadrupole and multiple-collector ICP-MS. *Chemical Geology*, *247*(1-2), 100-118.

Zheng, Y. F., Fu, B., Gong, B., & Li, L. (2003). Stable isotope geochemistry of ultrahigh pressure metamorphic rocks from the Dabie–Sulu orogen in China: implications for geodynamics and fluid regime. *Earth-Science Reviews*, *62*(1-2), 105-161.

Zheng, Y. F., Wu, Y. B., Zhao, Z. F., Zhang, S. B., Xu, P., & Wu, F. Y. (2005). Metamorphic effect on zircon Lu–Hf and U–Pb isotope systems in ultrahigh-pressure eclogite-facies metagranite and metabasite. *Earth and Planetary Science Letters, 240*(2), 378-400.

Zheng, Y. F., Gao, T. S., Wu, Y. B., Gong, B., & Liu, X. M. (2007). Fluid flow during exhumation of deeply subducted continental crust: zircon U-Pb age and O-isotope studies of a quartz vein within ultrahigh-pressure eclogite. *Journal of Metamorphic Geology*, *25*(2), 267-283.

Zlatkin, O., Avigad, D., & Gerdes, A. (2018). New detrital zircon geochronology from the Cycladic Basement (Greece): Implications for the Paleozoic accretion of peri-Gondwanan terranes to Laurussia. *Tectonics*, *37*(12), 4679-4699.